



UPPSALA
UNIVERSITET

*Digital Comprehensive Summaries of Uppsala Dissertations
from the Faculty of Science and Technology 726*

Neutron Spectrometry Techniques for Fusion Plasmas

Instrumentation and Performance

ERIK ANDERSSON SUNDÉN



ACTA
UNIVERSITATIS
UPSALIENSIS
UPPSALA
2010

ISSN 1651-6214
ISBN 978-91-554-7767-7
urn:nbn:se:uu:diva-121615

Dissertation presented at Uppsala University to be publicly examined in Högssalen, Angstrom Laboratory, Lagerhyddsvägen 1, Uppsala, Wednesday, May 12, 2010 at 10:15 for the degree of Doctor of Philosophy. The examination will be conducted in English.

Abstract

Andersson Sundén, E. 2010. Neutron Spectrometry Techniques for Fusion Plasmas. Instrumentation and Performance. Acta Universitatis Upsaliensis. *Digital Comprehensive Summaries of Uppsala Dissertations from the Faculty of Science and Technology* 726. 70 pp. Uppsala. ISBN 978-91-554-7767-7.

Neutrons are emitted from a deuterium plasma with energies around 2.5 MeV. The neutron spectrum is intimately related to the ion velocity distribution of the plasma. As a consequence, the analysis of neutron energy spectra can give information of the plasma rotation, the ion temperature, heating efficiency and fusion power.

The upgraded magnetic proton recoil spectrometer (MPRu), based on the thin-foil technique, is installed at the tokamak JET. The upgrade of the spectrometer was done to allow for measurements of deuterium plasmas. This thesis describes the hardware, the data reduction scheme and the kind of fusion plasma parameters that can be estimated from the data of the MPRu. The MPRu data from 3rd harmonic ion cyclotron resonance and beam heating are studied.

Other neutron spectrometer techniques are reviewed as well, in particular in the aspect of suitability for neutron emission spectrometry at ITER. Each spectrometer technique is evaluated using synthetic data which is obtained from standard scenarios of ITER. From this evaluation, we conclude that the thin-foil technique is the best technique to measure, e.g., the ion temperature in terms of time resolution.

Keywords: fusion, plasma diagnostics, neutron spectrometry, neutron spectroscopy, MPRu, magnetic proton recoil spectrometer, fusion, ITER

Erik Andersson Sundén, Department of Physics and Astronomy, Applied Nuclear Physics, Box 516, Uppsala University, SE-751 20 Uppsala, Sweden

© Erik Andersson Sundén 2010

ISSN 1651-6214

ISBN 978-91-554-7767-7

urn:nbn:se:uu:diva-121615 (<http://urn.kb.se/resolve?urn=urn:nbn:se:uu:diva-121615>)

Till Therese

List of Papers

This thesis is based on the following papers, which are referred to in the text by their Roman numerals.

- I **The thin-foil magnetic proton recoil spectrometer MPRu at JET**
Andersson Sundén, E., Sjöstrand, H., Conroy, S., Ericsson, G., Gatu Johnson, M., Giacomelli, L., Hellesen, C., Hjalmarsson, A., Ronchi, E., Weiszflog, M., Källne, J., Gorini, G., Tardocchi, M., Combo, A., Cruz, N., Batista, A., Pereira, R., Fortuna, R., Sousa, J., Popovichev, S. and JET-EFDA contributors
Nuclear Instruments and Methods in Physics Research A, (2009) 610:682-699
My contribution: Participated in the assembly of the instrument, designed the data acquisition program and wrote the paper.
- II **Gain stabilization control system of the upgraded magnetic proton recoil neutron spectrometer at JET**
Sjöstrand, H., Andersson Sundén, E., Conroy, S., Ericsson, G., Gatu Johnson, M., Giacomelli, L., Gorini, G., Hellesen, C., Hjalmarsson, A., Popovichev, S., Ronchi, E., Weiszflog, M., Tardocchi, M. and JET-EFDA contributors
Review of Scientific Instruments, (2008) 80:063505
My contribution: Participated in the design of the data reduction techniques and actively participated in the design process of the gain stabilization program.
- III **Neutron emission spectroscopy diagnosis of JET D plasmas with the new MPRu instrument**
Andersson Sundén, E., Conroy, S., Ericsson, G., Gatu Johnson, M., Giacomelli, L., Hellesen, C., Hjalmarsson, A., Källne, J., Ronchi, E., Sjöstrand, H., Weiszflog, M., Gorini, G., Tardocchi, M., Murari, A., Popovichev, S., Sousa, J., Pereira, R.C., Combo, A., Cruz, N. and JET EFDA contributors
33rd EPS Conference on Plasma Phys., (2006) ECA 30I 1.071
My contribution: Analysed the data and wrote the paper.
- IV **Evaluation of spectral unfolding techniques for neutron spectroscopy**
Andersson Sundén, E., Conroy, S., Ericsson, G., Gatu Johnson, M., Giacomelli, L., Hellesen, C., Hjalmarsson, A., Källne, J., Ronchi, E., Sjö-

trand, H., Weiszflog, M., Gorini, G., Tardocchi, M. and JET EFDA contributors

Proceedings of the International Workshop on Burning Plasma Diagnostics, (2007) Varenna Italy

My contribution: Wrote the paper and performed the simulations.

- V **Instrumentation for neutron emission spectrometry in use at JET** Andersson Sundén, E., Ericsson, G., Cecconello, M., Conroy, S., Gatu Johnson, M., Giacomelli, L., Hellesen, C., Hjalmarsson, A., Källne, J., Ronchi, E., Sangaroon, S., Sjöstrand, H., Weiszflog, M. and JET-EFDA Contributors

Proceedings of the International Conference on Frontiers in Diagnostic Technologies, (2009) Rome, Italy, doi:10.1016/j.nima.2010.02.255

My contribution: Wrote the paper and discussed the content on the conference.

- VI **Properties of neutron emission spectrometers at ITER** Andersson Sundén, E., Ballabio, L. , Ericsson, G., Cecconello, M., Conroy, S., Gatu Johnson, M., Gorini, G., Hellesen, C., Ognissanto, F., Ronchi, E., Sjöstrand, H., Tardocchi, M. and Weiszflog, M..

To be submitted to Fusion Tech. & Design

My contribution: Simulated the synthetic instrument response functions, performed the simulations and wrote the paper.

Reprints were made with permission from the publishers.

Contents

1	Nuclear fusion	9
1.1	Introduction	9
1.2	Magnetic confinement	12
1.2.1	Plasma heating	13
2	Neutron measurements	15
2.1	Neutron Flux Measurements	15
2.1.1	Activation foils	16
2.1.2	Fission chambers	16
2.1.3	Neutron emission profile measurements	16
2.2	Neutron spectrometry	16
2.2.1	Organic Scintillators	18
2.2.2	Semiconductors	19
2.2.3	Time-of-flight spectrometers	19
2.2.4	Thin-foil spectrometers	21
3	The upgraded magnetic proton recoil spectrometer	25
3.1	Data reduction	30
3.1.1	Baseline restoration	30
3.1.2	Event identification and selection	32
3.1.3	Background reduction	33
3.1.4	Gain correction	35
4	Data interpretation	39
4.1	Forward convolution method	39
4.1.1	Magnetic proton recoil spectrometer data	40
4.1.2	Fusion power measurements of deuterium plasmas using a neutron camera-spectrometer system	47
4.2	Unfolding methods	49
4.3	Evaluation procedure using synthetic data	52
4.3.1	Evaluation of instrument response functions	54
4.3.2	Evaluation of unfolding techniques	54
5	Conclusions	61
6	Summary in swedish	63
7	Acknowledgements	65
	Bibliography	67

1. Nuclear fusion

1.1 Introduction

Fusion experiments seek to release energy by fusing light nuclei. Tritium (t) and deuterium (d) are good candidates as fuels in future fusion reactors. Table 1.1 shows the fusion reactions available from such fuel, together with their Q -values and neutron energies, E_n , where applicable. The dt reaction (no. 4 in Table 1.1) has the highest reactivity, $\langle\sigma v\rangle$, for most temperatures of relevance for fusion energy research. The reactivity is given by

$$\langle\sigma v\rangle_{ij} = \iint f_i(v_i)f_j(v_j)|v_i - v_j|\sigma(|v_i - v_j|)d^3v_i d^3v_j \quad (1.1)$$

where i and j indicates the reactant species, v_i is the velocity of reactant i , $f_i(v_i)$ is the normalised ion velocity distribution of reactant i and $\sigma(|v_i - v_j|)$ is the reaction cross-section as a function of the relative velocity of the ions. The high reactivity for the d+t reaction, compared to the other reactions is shown in Figure 1.1.

An ion species in thermal equilibrium has a Maxwellian velocity distribution

$$f(v) = \left(\frac{m}{2\pi T_i}\right)^{\frac{3}{2}} \exp\left[-\frac{mv^2}{2T_i}\right], \quad (1.2)$$

where m is the ion mass and T_i is the ion temperature. Temperatures in plasma research are traditionally multiplied by Boltzmann's constant resulting in a quantity of unit energy. In this thesis, temperatures are discussed in terms of keV using this relation but omitting the constant. Thus, an ion temperature of 10^8 K corresponds to T_i of about 10 keV. The deuterium and tritium atoms (D

Table 1.1: *Reactions of deuterium and tritium together with the corresponding Q values, neutron energies, E_n , and branching ratios, β , where applicable.*

	Reaction	Q [MeV]	E_n [MeV]	β
1.	d(d,n) ³ He	3.3	2.45	0.5
2.	d(d,p)t	4.0	-	0.5
3.	³ He(d,p) ⁴ He	18.4	-	1.0
4.	d(t,n) ⁴ He	17.6	14.0	1.0

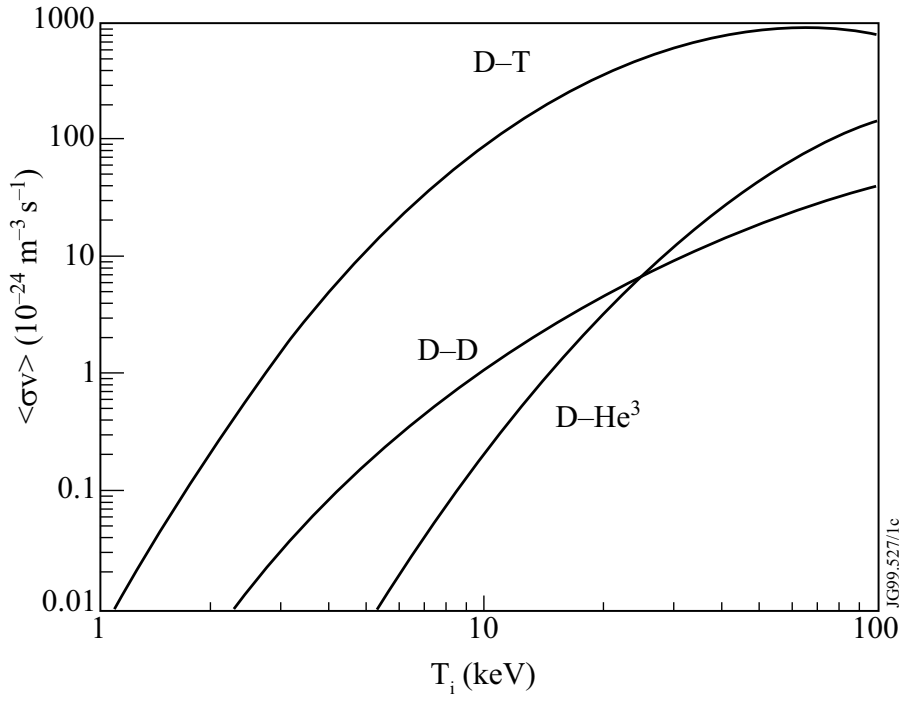


Figure 1.1: The reactivity for a plasma in thermal equilibrium as a function of the ion temperature for reaction 1+2 (combined), 3 and 4 in Table 1.1. ©EFDA-JET

and T) are ionised in the temperature region of interest for a fusion reactor. The ions together with the electrons constitute a fusion plasma. A plasma can be considered as two intermixed fluids, one describing the motion of the ions and the other one that of the electrons.

Energy ("heat") is transferred to the plasma from external sources, as described in some detail below, or internally from energy released in the fusion reactions. The d+t reaction results in an α -particle and a neutron. The 14.0 MeV neutron leaves the plasma. The 3.5 MeV α -particle, on the other hand, is here assumed to deposit its energy to the plasma by collisions with the plasma electrons and ions. Let us consider the power balance of a plasma of 50% D and 50% T, i.e. $n_d = n_t = n/2$, where n is the number density. Assuming a steady state we have

$$P_H + P_\alpha = P_L \quad (1.3)$$

where P_H is the external heating, P_α is the internal heating by the α -particles and P_L is the power loss of the plasma due to transport mechanisms. The average energy of a particle of temperature T is $3nT/2$ and, since we have both electrons and ions, the total energy density of a plasma in thermal equilibrium is $3nT$ [1]. The power loss from transport is then defined as

$$P_L = \frac{3nT}{\tau_E} V, \quad (1.4)$$

where V is the plasma volume and τ_E is the energy confinement time, which characterises the confinement of the plasma energy. The internal heating by the α -particles is proportional to the number of particles produced and their energy, E_α ,

$$P_\alpha = \frac{1}{4} n^2 \langle \sigma v \rangle E_\alpha V. \quad (1.5)$$

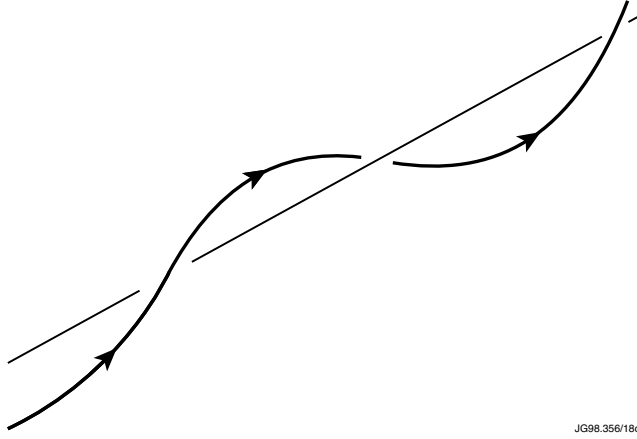
In the temperature range $10 \text{ keV} < T_i < 20 \text{ keV}$ the reactivity can be approximated as

$$\langle \sigma v \rangle = 1.1 \cdot 10^{-24} \cdot T_i^2 m^3 / s, \quad (1.6)$$

where T_i is in keV. This relation gives the ignition criterion expressed as the *triple product*,

$$nT \tau_E > 5 \cdot 10^{21} m^{-3} keVs. \quad (1.7)$$

Obviously, it is of great importance to know the quantities of the triple product. This thesis describes neutron emission spectroscopy as a tool to give such information.



JG98.356/18c

Figure 1.2: Illustration of a trajectory of an electrically charged particle (line with arrows) spiralling around a magnetic field line (straight line). ©EFDA-JET

1.2 Magnetic confinement

In the presence of a magnetic field, the velocity, \vec{v} , of an electrically charged particle can be divided into two components: one parallel, v_{\parallel} , and one perpendicular, v_{\perp} , to the magnetic field. The perpendicular velocity causes the particle to rotate around the field line (Figure 1.2) due to the Lorentz force,

$$\vec{F}_{\text{Lorentz}} = q(\vec{v} \times \vec{B}), \quad (1.8)$$

where \vec{B} is the magnetic field and q is the charge of the particle. Thus, a magnetic field confines the particles along the field line. The particle will gyrate around the magnetic field with a so called Larmor radius of

$$\rho_L = \frac{mv_{\perp}}{|q|B} \quad (1.9)$$

and the angular (cyclotron) frequency of the gyration will be

$$\omega_c = \frac{v_{\perp}}{\rho_L} = \frac{qB}{m}. \quad (1.10)$$

To fully enclose the plasma, an intuitive solution to the confinement problem is to ‘bend’ the magnetic field to a circle. This solution is used in the reactor concept tokamak, where the circular magnetic field is called the toroidal field, B_t , which is proportional to the inverse of the major radius, R_{major} . It can be shown that the toroidal magnetic field is not sufficient to confine the plasma. In addition, a poloidal field, B_p , is needed, which is obtained by inducing a toroidal current through the plasma itself. The superimposed poloidal and toroidal fields result in a helical magnetic field, which can confine the

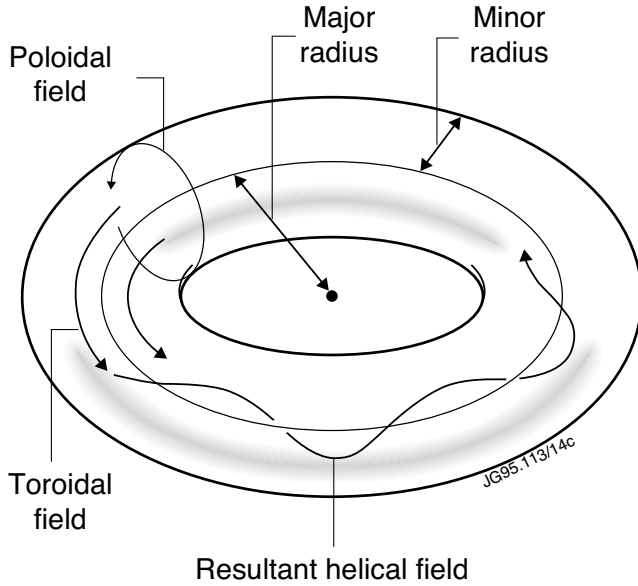


Figure 1.3: Overview of the magnetic field components of a tokamak reactor. ©EFDA-JET

plasma. The magnetic field configuration of the tokamak concept is illustrated in Figure 1.3.

At present, the largest tokamak in the world is JET located outside Oxford, United Kingdom. The minor radius, R_{minor} , is 1 m and R_{major} is 3 m resulting in a total plasma volume of about 100 m^3 . JET has the highest achieved power output of all tokamaks so far, peaking at a value of 16 MW [2]. The plasma of this record JET pulse was in DT operation with a triple product of $8.7 \cdot 10^{20}$ [3], i.e., still a factor of about six below that of the ignition criterion expressed in Equation 1.7.

The next step towards commercial tokamak reactors, ITER, is presently being built in Cadarache, France. The first plasma of ITER is planned for 2019. The major radius will be 6 m and the inner radius 2 m resulting in a plasma volume of 840 m^3 . The aim of ITER is to produce 500 MW of fusion power and to release 10 times more energy than is externally being transferred into the plasma [4].

1.2.1 Plasma heating

A tokamak plasma can be externally heated in addition to the internal heating of the α -particles. There are at present three main heating systems available for external heating: the Ohmic, the neutral beam injection (NBI) and the radio frequency (RF) heating. There are several types of RF heating and here we will only discuss ion cyclotron resonance frequency heating (ICRH).

The toroidal current, which is the source of the poloidal field, provides heating due to the resistivity of the plasma. This heating is called Ohmic heating. Ohmic heating can only raise the temperature of the plasma up to a few keV. This limitation is due to a decrease in resistivity with increased electron temperature, T_e .

A beam of high energy neutral atoms, such as D or T, can be injected into the plasma. This injection serves two purposes; firstly, it feeds the reactor plasma with new ions to fuse and, secondly, the energy of the beam ions is deposited in the plasma by beam ion collisions with the electrons and ions of the bulk plasma. This heating is called NBI heating. The beam energies at JET are 80 to 130 keV and are planned to be 1 MeV at ITER.

A third external heating system is that of ICRH. ICRH relies on electromagnetic waves transferring power to the plasma at specific frequencies. These ICRH frequencies, ω , are chosen to match the cyclotron frequency of a specific fuel ion at a specific location in the plasma. This location can be chosen using the fact that $B_t \propto 1/R_{\text{major}}$ and consequently $\omega_c \propto 1/R_{\text{major}}$ (see Equation 1.10).

2. Neutron measurements

Neutrons are hard to detect directly, since they are uncharged. This is why neutron measurement techniques often “convert” the uncharged neutrons to charged particles, which in turn are measured. In this chapter two measurements of neutrons are considered: the neutron flux and the neutron energy.

2.1 Neutron Flux Measurements

The neutron emission is important to monitor since the energetic neutrons tend to activate the surrounding material of the plasma. The neutron emission per volume element, y_n , with d and/or t present in the plasma is

$$y_{n,2.5\text{MeV}}(R, Z, \varphi) = \frac{n_d^2}{2} \langle \sigma v \rangle_{d,d} \quad (2.1)$$

and

$$y_{n,14\text{MeV}}(R, Z, \varphi) = n_d n_t \langle \sigma v \rangle_{d,t}, \quad (2.2)$$

where n_i is the number density of species i and $\langle \sigma v \rangle_{i,j}$ is the reactivity for species i and j , described in Equation 1.1. The neutron rate, Y_n , is obtained by integrating these quantities over the plasma volume

$$Y_n = \int_V y_n dV. \quad (2.3)$$

where V is the total volume of the plasma. The fusion power, P_{fusion} , is directly proportional to the neutron emission rate as

$$P_{\text{fusion}} = Q_{dt} Y_{n,14\text{MeV}} + Y_{n,2.5\text{MeV}} \left(Q_{dd,1} + Q_{dd,2} \frac{\beta_2}{\beta_1} \right) \quad (2.4)$$

where Q and β refers to the Q values and branching ratios given in Table 1.1, respectively. Since P_{fusion} is a measure of the performance of the energy production, it is of great importance to measure the neutron fluxes from a tokamak.

In Section 4.1.2, a novel method of measuring the neutron yield, and by extension the fusion power, is presented. In this section we describe three

neutron flux measurement techniques: activation foils, fission chambers and , finally, we briefly describe the neutron camera.

2.1.1 Activation foils

Activation foils are irradiated with neutrons and some nuclei are excited due to neutron absorption. After irradiation, the radioactive decay of the excited nuclei is measured. The neutron flux can be deduced by knowing the elapsed time since irradiation, the decay branches and the corresponding half-lives of the excited nuclei. Activation foils provides time-integrated measurements.

Activation foils have been used at JET[5], TFTR[6] and JT-60U[7] for absolute measurements of the neutron flux.

2.1.2 Fission chambers

Fission chambers are used for time-resolved neutron flux measurements. Fission chambers consist of a thin fissionable film, typically of a material containing an Uranium isotope, and an ionisation chamber. The neutrons induce fission of the nuclei in the film and the fission products are detected in the ionisation chamber. This technique is sensitive to the relative change in the neutron flux and can cover 10 orders of magnitude in intensity.

Fission chambers have been *in situ* calibrated at JET [8], TFTR [9] and JT-60U[10] using ^{252}Cf and DT sources. *In situ* calibrations must be redone after each change of hardware in the reactor, in particular close to the fission chamber. This is why the more common way of calibrating the fission chambers is to cross calibrate them against activation foils.

2.1.3 Neutron emission profile measurements

The neutron emission profile of a tokamak plasma can be measured by a set of collimated flux detectors, a so called neutron camera. Such systems have been developed at JET [11] (9 vertical and 10 horizontal LOS), TFTR [12] (10 vertical LOS) and JT-60U [13] (6 diagonal LOS). The measured flux of the detectors can be used to determine the neutron emission profile by the forward convolution method, as described in Section 4.1.2, or by other unfolding techniques [14, 15].

2.2 Neutron spectrometry

The uncharged neutrons released in fusion reactions are unconstrained by the magnetic fields of a tokamak and leave the plasma confinement without further interaction. The energy of a neutron released in a fusion reaction is given

by [16]

$$E_n = \frac{m_n v_{\text{cm}}^2}{2} + \frac{m_R}{m_n + m_R} (Q + K) + v_{\text{cm}} \cos(\theta) \left(\frac{2m_n m_R}{m_n + m_R} (Q + K) \right)^{1/2}, \quad (2.5)$$

where m_n is the neutron mass, m_R is the mass of the residual nucleus, Q is the total energy released in the reaction, K is the relative energy and v_{cm} is the velocity of the centre of mass system. K and v_{cm} are defined as

$$K = \frac{\mu v_{\text{rel}}^2}{2}, \quad (2.6)$$

and

$$v_{\text{cm}} = \frac{m_1 v_1 + m_2 v_2}{m_1 + m_2}, \quad (2.7)$$

where v_{rel} is the relative velocity of the reactants resulting in the neutron, m_1 and m_2 are the masses of the reactants and μ is the reduced mass,

$$\mu = \frac{m_1 m_2}{m_1 + m_2}. \quad (2.8)$$

In Equation 2.5, the angle θ in the third term is that between the centre of mass velocity and the velocity of the emitted neutron in the centre of mass system.

The term of Equation 2.5 involving $\cos(\theta)$ is intimately connected to the angle of the line of sight of an observer, φ , relative to the magnetic field. In this thesis, the fusion reactions are observed by a neutron emission spectrometer. In addition to the pure two-body kinematics of Equation 2.5, the fusion plasma can exhibit a collective rotational motion inside the tokamak vessel. The energy shift, ΔE , of a toroidal rotation seen by a neutron spectrometer measuring the d+d or d+t reactions is

$$\Delta E = C_{\text{rot}} v_t \cos(\varphi), \quad (2.9)$$

where v_t is the toroidal rotation velocity and C_{rot} is 0.23 and 0.54 keV/(km/s) for the d+d and d+t reactions, respectively [17, 18].

From Equation 2.5 it can be seen that the neutron energy is highly affected by the velocity of the reactants. Neutron emission spectroscopy is therefore a valuable tool for measuring and understanding the underlying ion population energy distribution.

Let us consider three different types of fusion reactions; firstly, the so called “cold” plasma interaction, secondly, the reaction of a high energy beam deuterium ion fusing with a thermal tritium ion and, thirdly, the case of plasma ions in thermal equilibrium.

The “cold” plasma case corresponds to a plasma with low temperature, i.e., $K=0$ and $v_{cm}=0$ in Equation 2.5. The equation is then reduced to

$$E_n = \frac{m_R}{m_n + m_R} Q. \quad (2.10)$$

E_n is then the neutron energy given in Table 1.1, i.e., 2.45 MeV when the reactants are two deuterium ions and 14.0 MeV when the reactants are a tritium and a deuterium ion.

Now let us consider a deuterium beam ion that is injected with the kinetic energy 100 keV into a “cold” tritium plasma. Equation 2.5 shows that when a deuterium beam ion fuses with a tritium ion with no kinetic energy, the energy of the emitted neutron is in the range $13.4 \text{ MeV} < E_n < 14.8 \text{ MeV}$, where the minimum and maximum energies corresponds to $\cos(\theta)=-1$ and 1, respectively.

An ion population in thermal equilibrium is described by a Maxwell-Boltzmann distribution (Equation 1.2). The neutron energy spectrum, which originates from the thermal ion population interacting with itself, can be well approximated with a Gaussian [16]. The full width at half maximum (FWHM) of the Gaussian is proportional to the square root of the temperature of the plasma. The relation is

$$FWHM = C_T \sqrt{T_i}, \quad (2.11)$$

where C_T is $82.5 \text{ keV}^{1/2}$ and $177 \text{ keV}^{1/2}$ in the case of a D and DT plasma, respectively. In the case of non-Maxwellian distributions the neutron spectrum changes shape and must be calculated numerically.

The rest of this chapter is devoted to describe measurement techniques commonly used for neutron energy spectrometry. In Paper VI, several of these techniques are evaluated in terms of ITER requirements [19].

2.2.1 Organic Scintillators

Organic scintillators consist mainly of carbon and hydrogen. When used as neutron spectrometers, the collimated neutrons scatter elastically on the hydrogen producing recoil protons, which in turn are slowed down and detected. The neutron can deposit any amount of energy in the elastic scattering and consequently the mono-energetic response of an organic scintillator is rectangular-shaped. For some organic scintillators, the induced scintillator light pulse has a shape that is particle type dependent. This effect can be used for pulse-shape discrimination and allows for neutron energy measurements in, e.g., mixed neutron/ γ fields [20]. The efficiency of these detectors is high. However, the count-rate capability is limited by the gain stability and the long light pulses of the scintillators. Recent studies have reported count rates of

about 0.5 MHz with a gain stability of 1% [21]. This technique has been used at JET for neutron spectrum measurements, see e.g. [22, 23, 24].

2.2.2 Semiconductors

Semi-conductors can be used to detect neutrons by using intrinsic reaction channels of the material to indirectly measure the neutron energies. The charged particles created in the reaction will slow down in the detector and create a number of electron-hole pairs proportional to the neutron energy. Previously, Si semi-conductors have successfully been used as neutron spectrometers [25, 26]. However, in this thesis we focus on diamonds as a representative of the semi-conductors. Diamonds are well suited for neutron emission spectrometry, due to their radiation hardness, relatively high efficiency and good energy resolution ($FWHM/E_n=2-7\%$ [27, 28]). In Table 2.1, the available reaction channels for 14-MeV neutrons impinging on diamonds are presented. Reaction 5 is well suited for neutron emission spectroscopy since it results in only charged particles and the energy threshold, E_{th} , is low enough compared to the other reactions to separate these events in a pulse-height spectrum. In Paper VI, the IRF of diamonds is estimated from data of [27] and [29]. The resulting mono-energetic 14-MeV response is shown in Figure 2.1, where the Gaussian like peak corresponds to the $^{12}\text{C}(n,\alpha)^9\text{Be}$ reaction channel and the shoulder at lower pulse heights corresponds to reactions 3.1-3.5. The non-zero level between the two components can be explained by incomplete charge collection of the $^{12}\text{C}(n,\alpha)^9\text{Be}$ reaction. This technique is generally limited by the count-rate capability of the detector. In [30] the count rate for one diamond detector is estimated to 1 MHz. A segmentation of the detector would increase this to higher values. Also a shift from analogue to digital pulse-handling electronics could work in the same direction.

Diamonds have been used as neutron spectrometers at JET [31], TFTR [28] and JT-60U [32].

2.2.3 Time-of-flight spectrometers

Time-of-flight (TOF) spectrometers consist of two sets of detectors: the primary detectors and the secondary detectors, as illustrated in Figure 2.2. A collimated neutron beam intersects the primary detector, where neutrons scatter elastically in an angle θ . The scattered neutrons are detected in the secondary detector. The time of flight, t_{TOF} , between the detection of neutron events are recorded. The two detector sets are aligned to the, so called, constant TOF sphere with radius R . The energy of the scattered neutron, $E_{n'}$, is related to the

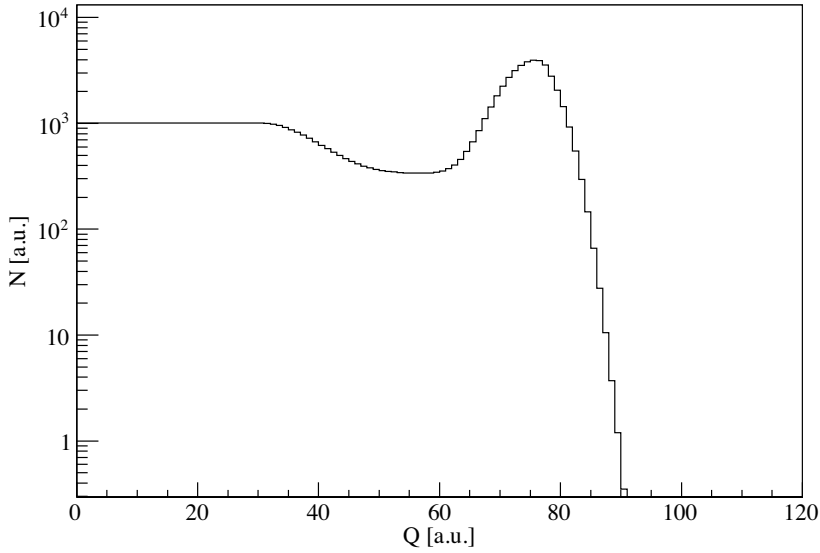


Figure 2.1: Simulated instrument response of a 14-MeV neutron for a diamond detector. (From Paper VI.)

Table 2.1: Reaction channels for neutrons impinging a diamond detector [27]. The cross sections are given for $E_n = 14\text{MeV}$

	Reaction	E_{th} [MeV]	σ [mb]	$E_{\text{excitation}}$ [MeV]
1.	$^{12}\text{C}(\text{n},\text{n}')^{12}\text{C}$	0.0	800	
2.	$^{12}\text{C}(\text{n},\text{n}')^{12}\text{C}^*$	4.8	200	4.44
3.	$^{12}\text{C}(\text{n},\text{n}')^{12}\text{C}^*(\alpha)$			
3.1		8.3	10	7.65
3.2		10.4	76	9.64
3.3		11.7	47	10.8
3.4		12.8	39	11.8
3.5		13.8	39	12.8
4.	$^{12}\text{C}(\text{n},\alpha)^9\text{Be}^*$	8.8	32	2.43
5.	$^{12}\text{C}(\text{n},\alpha)^9\text{Be}$	6.2	72	

incoming neutron energy, E_n , as

$$E_{n'} = E_n \cos^2(\theta) = \frac{m_n v_{n'}^2}{2} = \frac{m_n}{2} \left(\frac{L}{t_{\text{TOF}}} \right)^2, \quad (2.12)$$

where L is the length of the flight path. Realising that

$$L = 2R \cos(\theta) \quad (2.13)$$

gives us

$$E_n = \frac{2m_n R^2}{t_{\text{TOF}}^2}. \quad (2.14)$$

In Figure 2.2, note that the tip of the secondary detector is tilted towards the centre of the TOF sphere (and the base consequently away from the centre) to compensate for the time of the signals to arrive to the PMTs.

The TOF technique is mainly limited by its count-rate capability since the signal of a TOF spectrometer is proportional to the neutron flux and the random coincidences scale proportional to the square of the flux. As a consequence, the background-to-signal ratio (B/S) of the TOF technique increases linearly with the neutron flux to a level where the background totally overwhelms the signal.

This technique has been used at JET [33, 34, 35] and JT-60U [36] for neutron detection.

Recent developments in the data acquisition (DAQ) electronics allow for simultaneous storage of time and pulse height of each event in the TOF detectors. The pulse-height information can be used to reduce the random coincidences, as briefly discussed in Paper V. In Figure 2.3, the simulated response of a 14-MeV neutron with (red) and without (blue) such pulse-height discrimination is shown. This response is from a TOF spectrometer with a flight path of 2 m.

2.2.4 Thin-foil spectrometers

Thin foil spectrometers uses a hydrogen-rich (plastic) foil to convert collimated neutrons to recoil protons. The resulting proton energy, E_p , is

$$E_p = E_n \cos^2 \theta_{np}, \quad (2.15)$$

where E_n is the incoming neutron energy and θ_{np} is the angle of the velocity of the recoil proton relative to the velocity of the collimated neutron. In this thesis we describe two such systems: the thin foil proton recoil spectrometer (TPR) and the upgraded magnetic proton recoil spectrometer (MPRu). The latter is discussed in Chapter 3.

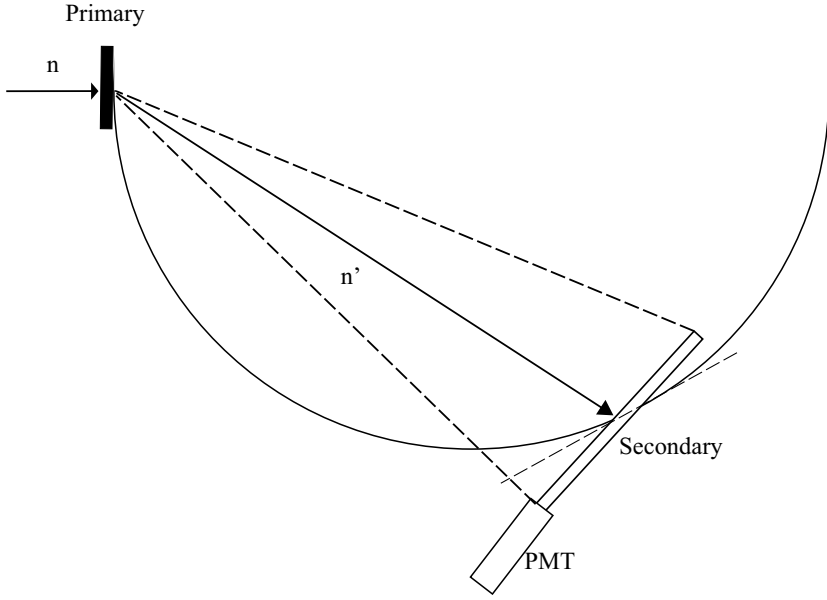


Figure 2.2: Principle sketch of the TOFOR spectrometer.

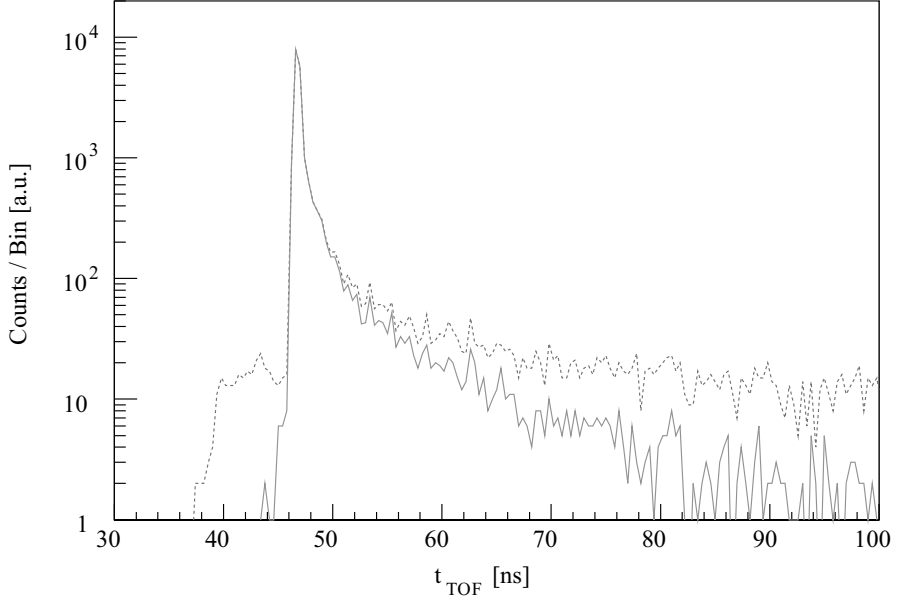


Figure 2.3: The mono-energetic response of a 14-MeV neutron for a time-of-flight spectrometer (red solid) with and (blue dashed) without pulse-height discrimination.

In the TPR technique [37, 38], protons scattered in a certain solid angle to the normal of the recoil foil impinges, e.g., a silicon detector. Energy determination of the protons is achieved by actively measuring their pulse-height spectrum in the detector. This technique has a low efficiency compared to the previously described techniques. However, the IRF of the TPR technique is close to a Gaussian [39] and has a good energy resolution. The technique was used at JET in the TANDEM system [37, 40] during the DTE1 campaign 1997. Tandem used an annular collimator with three foil-detector pairs placed after one another, achieving a total efficiency of 10^{-4} cm^2 and an energy resolution of 2.5% (FWHM/ E_n).

3. The upgraded magnetic proton recoil spectrometer

In Paper I, the hardware of the upgraded magnetic proton recoil spectrometer (MPRu) is presented together with some results collected during D operations at JET. In this chapter we discuss the hardware of the MPRu and expand a bit on the data reduction scheme used for the spectrometer data, since it is only briefly covered in Paper III.

The MPRu is installed at JET with a semi-tangential line of sight (LOS) passing through the plasma centre twice. The LOS has an inclination of 4.8° with respect to the equatorial plane of the torus and an angle, θ_{LOS} , of 47° with respect to the toroidal B-field in the centre of the tokamak [18]. The distance from the point on the LOS closest to the plasma centre to the foil of the MPRu is 8.9 m and the distance from the foil to the port in the vacuum vessel of JET is 4.3 m. Figure 3.1 is a schematic drawing of the MPRu and its subsystems installed at JET, including the radiation shielding.

Neutrons originating from the JET plasma enter the neutron collimator of the MPRu, which forms the divergent neutron flux into a “beam” entering the spectrometer. The neutron beam passes through a thin polythene foil (CH_2) where a fraction of the neutrons scatters elastically on the foil’s hydrogen nuclei (protons). This elastic scattering results in recoil protons with energies described by Equation 2.15. The forward scattered protons, with energies close to that of the scattered neutron, are selected by a circular proton collimator and enter the magnetic system of MPRu (Figure 3.2). The magnetic system has two tasks: firstly, it bends the proton trajectories about 150° away from the neutron beam and, secondly, it separates the protons spatially and focuses them onto a curved focal plane, indicated by a red curved line in Figure 3.2. A hodoscope, consisting of 32 phoswich scintillators, is placed at this focal plane. The resulting IRF of the MPRu is Gaussian like (see Figure 3.3). Two photo multiplier tubes (PMTs) are connected to each scintillator via light guides.

The phoswich scintillators of the hodoscope consist of two scintillating layers and, in some cases, a backing layer for improved light collection. The first scintillation layer facing the magnetic system is 0.3 mm thick and has a light decay time of 1.8 ns while the second scintillating layer is 2.3-3.2 mm thick with a decay time of 180 ns. The thickness of the second layer depends on the position of the scintillator in the hodoscope; a thinner layer for the scintillators at the low-energy proton side of the hodoscope and a thicker layer

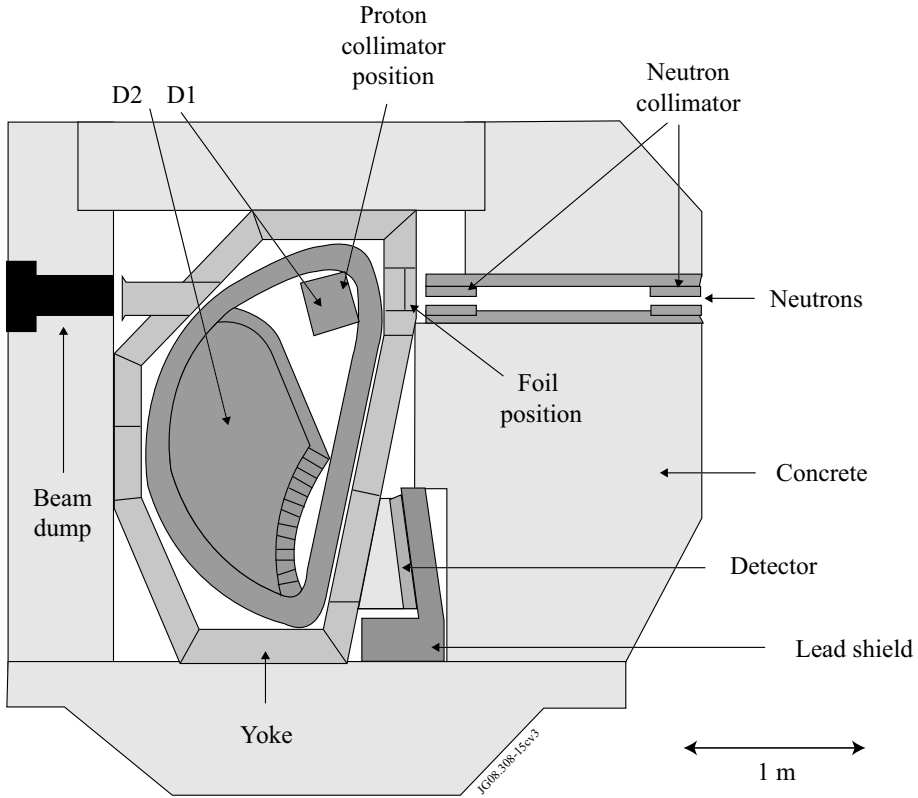


Figure 3.1: The components of the MPRu. ©EFDA-JET

for the scintillators at the high energy side. The total thickness has been chosen to correspond to the range of recoil protons when the magnet is tuned for 14-MeV measurements. A 2.45-MeV proton has a range of about 0.1 mm in plastic and thus deposits all of its energy in the thin scintillator layer; up to 4.7-MeV protons are stopped in the thin layer. A 14.0-MeV proton, with a range of about 2.2 mm in plastic, deposits part of its energy in the thin layer and the rests in the thick layer. This will result in two distinctly different pulse-shape signatures for the two proton energies of interest here, namely, 2.45 and 14.0 MeV. Particles and photons of other origins than the recoil protons, i.e., background, have other pulse-shape signatures. The energy and particle type dependent pulse shapes are used to distinguish the signal protons from the background.

For each phoswich scintillator the waveforms from the two connected PMTs are summed and amplified in a pulse summing amplifier (PSA) and then transmitted to a digital transient recorder card (TRC). Both the PSAs and the TRCs are custom-built for this application. The TRCs digitise and store the waveforms and their time stamps to allow for offline analysis. The

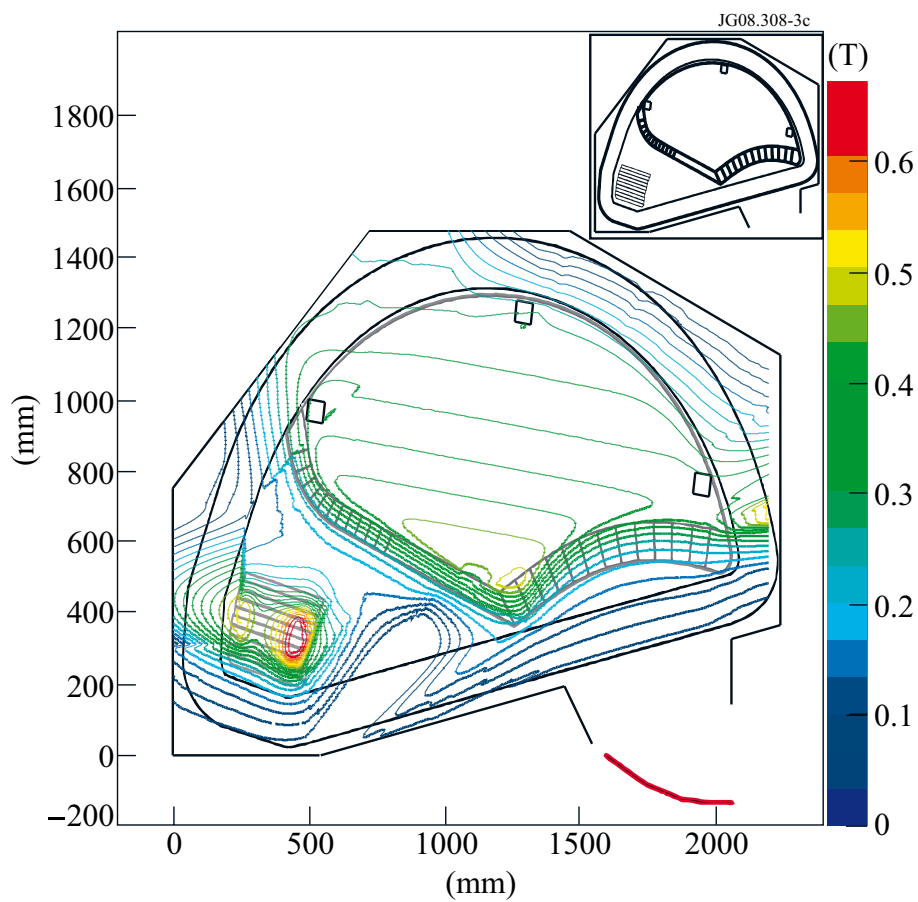


Figure 3.2: The magnetic field of a 2.5-MeV setting of the MPRu. ©EFDA-JET

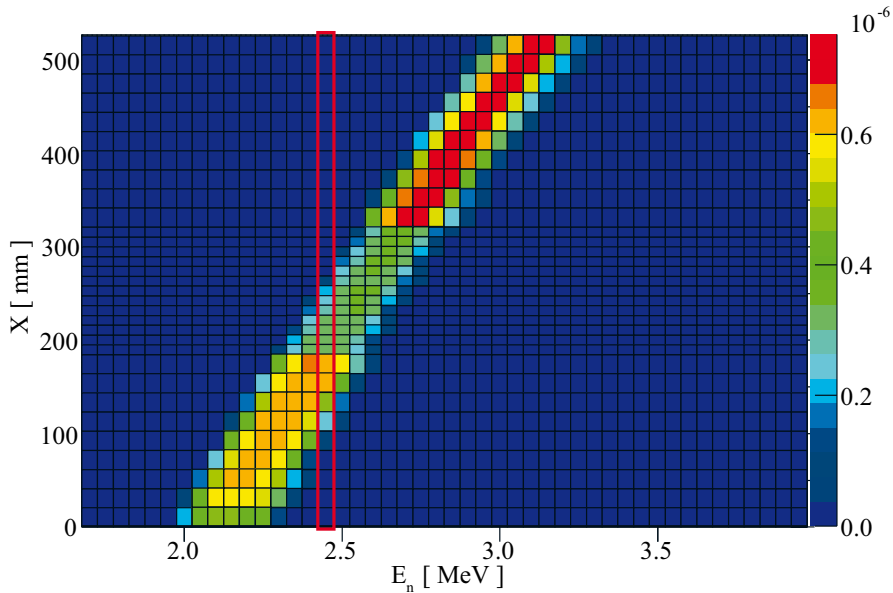


Figure 3.3: The IRF of a MPRu setting for 2.5-MeV measurements. The mono-energetic 2.45-MeV neutron response is enclosed by a red rectangle.

waveform together with its time stamp is referred to as a scintillator event. Each TRC has four input channels, each with an input voltage range of 0 to -1 V over a 50 Ω impedance. The waveform digitisation is done with 8 bit resolution at 200 MHz sampling frequency. Each TRC channel is triggered individually based on a pre-set voltage level.

The hodoscope channel corresponding to the lowest proton energy serves also as reference detector for Control and Monitoring (C&M) purposes. The signal processing chain of the C&M channel has some additional features, compared to the other channels, as shown in Figure 3.4. Scintillators of Yttrium Aluminium Perovskite doped with Cerium (YAP) with embedded α -emitting radioactive sources (^{241}Am) are illuminating the photocathode of the PMTs of the C&M channel. These signals are used as an absolute reference in the gain correction system. Furthermore, each phoswich scintillator is connected to a set of controlled light sources (CLSs) via an optical fibre. The amount of light collected in the C&M channel from the CLS and the YAP source is compared to determine possible variations in the electronic gain, here referred to as gain drifts. In addition to the YAP and CLS signals, the C&M channel also has a logic pulse from a 1 Hz JET clock unit added to the signal chain via a fan in/fan out (FIFO) module. This is used to relate the time of JET to that of the MPRu system. These C&M signals have distinct pulse shapes and frequencies and can easily be distinguished from the signals

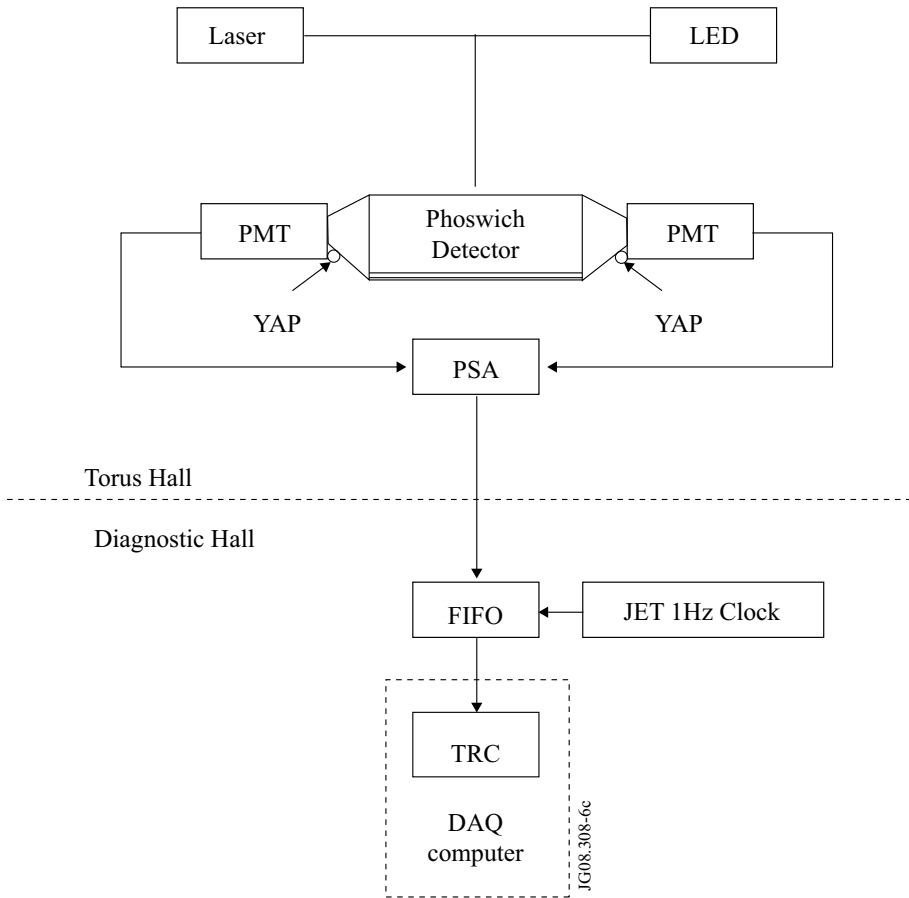


Figure 3.4: Overview of signal chain for the Control and Monitoring channel, where lines between blocks indicate the optical and electrical connections. All other phoswich scintillators have the same signal chain, but do not include the YAP sources, the FIFO and the JET 1 Hz clock.

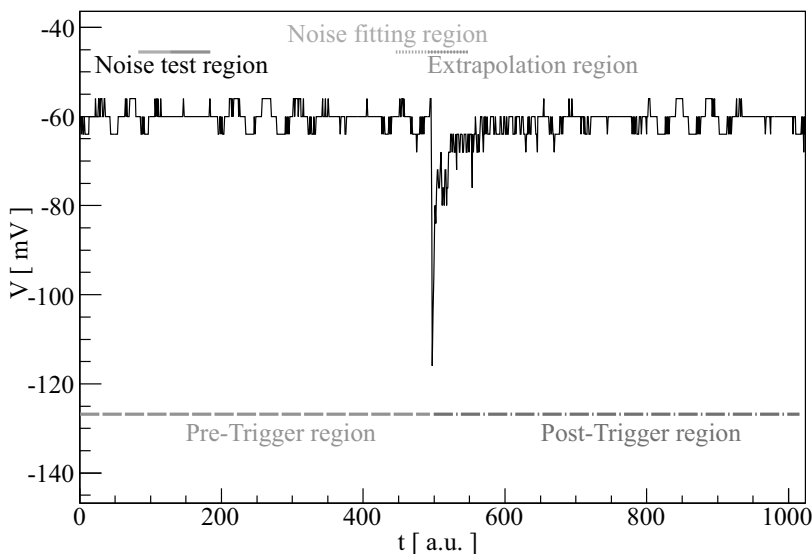


Figure 3.5: The full waveform of a scintillator event as registered by the TRC (black line). The coloured lines indicate different time regions used in the baseline restoration analysis.

originating from particles interacting in the phoswich scintillators (see Paper II).

3.1 Data reduction

The different C&M and hodoscope signals of the MPRu system are stored in the data acquisition computers. Several steps of data reduction are performed on the waveform data from the TRCs. These steps are baseline restoration, event identification and selection, background reduction and gain correction. Each step is discussed in some detail below and in paper III.

3.1.1 Baseline restoration

The waveform of a scintillator event can possibly have several components added to it, besides the one originating from a particle interaction in the scintillator. For example, the waveforms from the PMTs are intentionally shifted by a small value in the PSAs before they are summed and amplified. External pick-up in the signal chain is common, as well. This pick-up results in repetitive sinusoidal-like components as well as transients. In addition, an internal electronic noise is present.

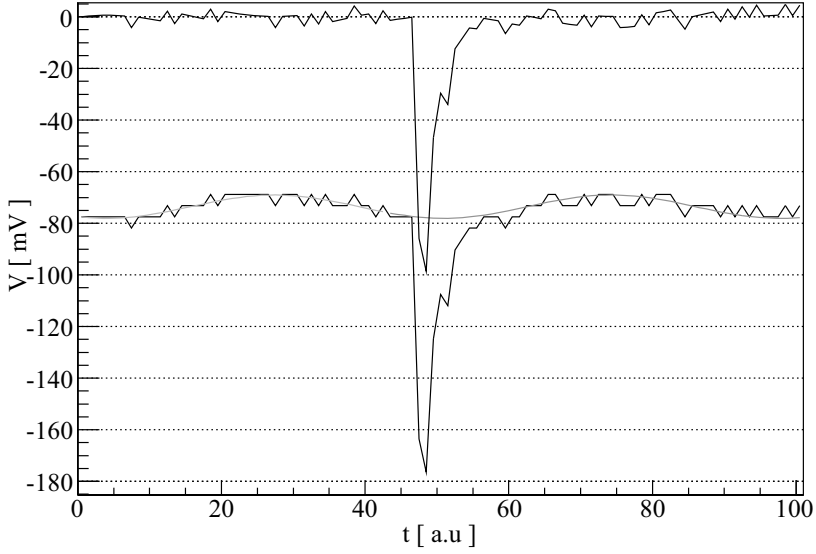


Figure 3.6: Typical waveform generated by a proton ($E_p < 4.5$ MeV) interacting in a phoswich scintillator. The lower black curve shows the noise fitting region ($t=0-45$ a.u.) and the extrapolation region ($t=45-100$ a.u.) of an original waveform, the upper black curve shows the situation after baseline restoration. In this example, a sinusoidal function is fitted to the noise fitting region (green line) and extrapolated into the extrapolation region (red line). The baseline restored waveform is obtained by subtracting the fitted noise function from the original waveform.

The waveform of each scintillator event consists of a pre- and a post-trigger region (Figure 3.5). Two parts of the pre-trigger region are used; the noise test region, at an early part of the waveform well separated from the noise fitting region; and the noise fitting region, in immediate contact with the post-trigger region. The waveform dataset of each hodoscope channel is analysed twice. Firstly, each of three baseline restoration techniques, as described below, is applied to the noise test region to determine the best baseline restoration technique to use. In a second step, the chosen baseline restoration technique is applied to the noise fitting region and the result is extrapolated into the extrapolation region.

Three different baseline restoration techniques are used to estimate the baseline shape for each waveform:

- I *The mean value technique:* The mean voltage value in the noise fitting region is calculated. This technique is used for channels without (or with small) pick-up.

- II *The straight line technique:* A straight line is fitted to the noise fitting region and extrapolated into the post-trigger region. This technique is used when the pick-up is a low frequency oscillation.
- III *The sinus technique:* A fast Fourier transform (FFT) method finds the most dominant frequency of the noise fitting region. The dominant frequency is set as initial value in an iterative fitting procedure to find the best sinusoidal function to describe the waveform in the noise fitting region. The fitted sinusoidal function is extrapolated into the post-trigger region. This technique is illustrated in Figure 3.6 and will be used for high frequency pick-up.

To determine what technique to use for a specific hodoscope channel the noise test region is divided into two regions: the first of the same length as the noise fitting region and the second of the same length as the extrapolation region. For each waveform of a dataset of each hodoscope channel, the following procedure is done:

1. Apply all three techniques to the first interval of the noise test region and extrapolate the results into the second interval.
2. Subtract the extrapolated result from the waveform data in the second interval for each technique.
3. Calculate the standard deviation of the restored baseline, assuming a mean value of zero, in the second interval for each technique.
4. Compare the standard deviation for the different techniques. The technique with the lowest value scores a point for this waveform. Keep a record of accumulated scores for each individual hodoscope channel and technique.

The technique with the highest score is used on the same dataset. In this way, we select the baseline restoration technique that performs best, given the prevailing pick-up situation for the studied dataset.

For a typical JET pulse (68000) the frequency of chosen baseline technique for the 32 different hodoscope channels are 18 (56%) for the mean value, 3 (9%) for the straight line and 11 (34%) for the sinus technique.

3.1.2 Event identification and selection

The next step in the data reduction process is event identification and selection. This selection is based on a detailed analysis of the shape of each waveform (also referred to as pulse shape discrimination, PSD). The baseline-restored waveforms are analysed by applying two integrating gates, resulting in two charge values, Q_{long} and Q_{short} , as depicted in Figure 3.7 for a proton-induced event.

The CLS and YAP events need occasionally to be separated from the other waveforms, e.g., in the gain shift calculations (further discussed below). The first step in this separation procedure is to calculate the average waveforms of the CLS and the YAP. The sample correlation coefficient, r , is calculated for each individual waveform with respect to the average waveforms of the CLS

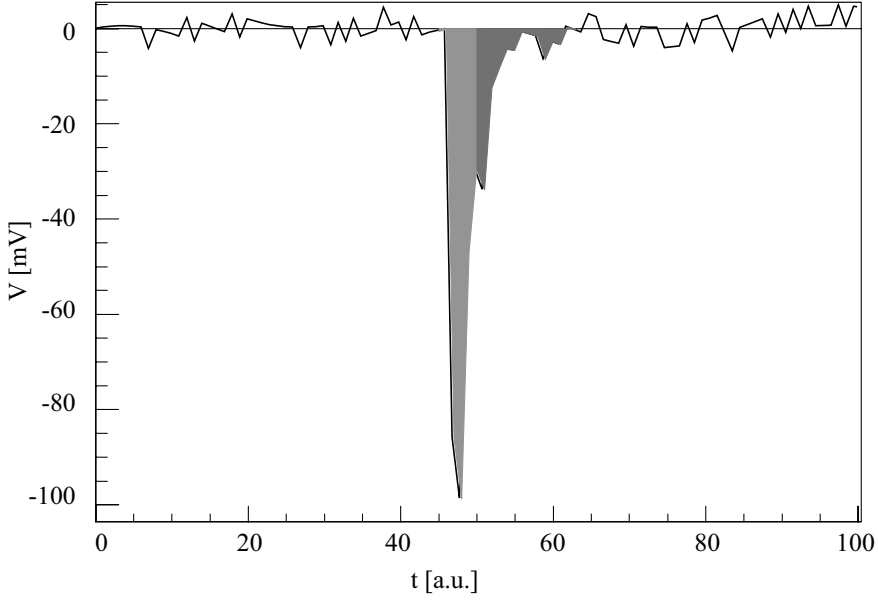


Figure 3.7: Baseline-restored proton-induced waveform with short (red) and long (blue) integration regions (gates) indicated.

and YAP.

$$r = \frac{\sum_{i=1}^n (y_{i,\text{data}} - \bar{y}_{\text{data}})(y_{i,\text{standard}} - \bar{y}_{\text{standard}})}{(n-1)\sigma_{\text{data}}\sigma_{\text{standard}}}, \quad (3.1)$$

where n is the number of bins in the waveform, $y_{i,\text{data}}$ and $y_{i,\text{standard}}$ are bin values, \bar{y}_{data} and $\bar{y}_{\text{standard}}$ are the mean values and σ_{data} and σ_{standard} are the standard deviations of the waveforms. The sample correlation coefficient is 1 if the two waveforms are identical and 0 if they are uncorrelated. If, for a specific waveform, r of one waveform is above 0.95 with respect to one of the average waveforms (CLS or YAP) it is assumed to be of that type.

3.1.3 Background reduction

For events due to physical particles interacting in the scintillators, the main benefit of the PSD analysis is a drastic reduction in the amount of background events in the data set. In this case, the short gate covers the main peak of the waveform and consequently mostly contains the signal generated in the thin layer of the phoswich scintillator. The long gate integrates the part of the waveform after the short gate and contains signal originating from both phoswich layers.

A $Q_{\text{long}}, Q_{\text{short}}$ distribution from several hundred summed JET pulses for a single phoswich scintillator is shown in Figures 3.9 and 3.10, with the spectrometer's magnet set to measure 2.45-MeV protons, as well as for a case with

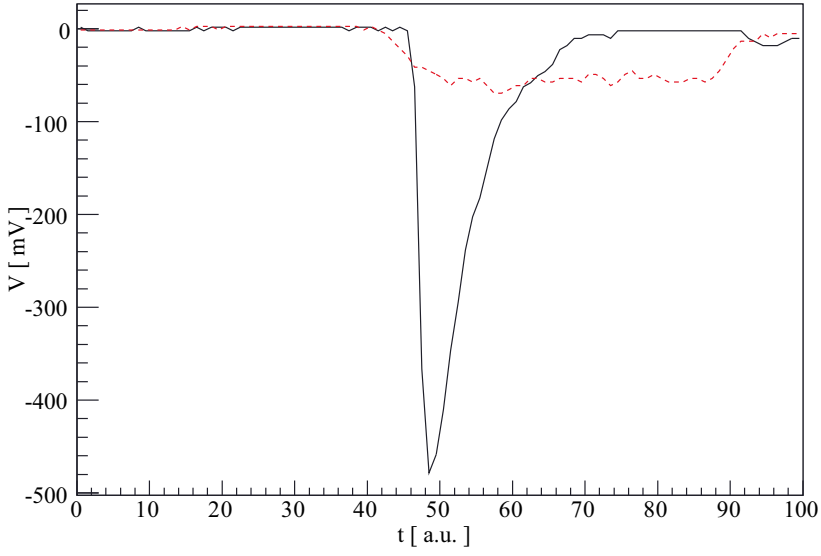


Figure 3.8: Baseline restored YAP (black solid line) and LED (red dashed line) waveforms.

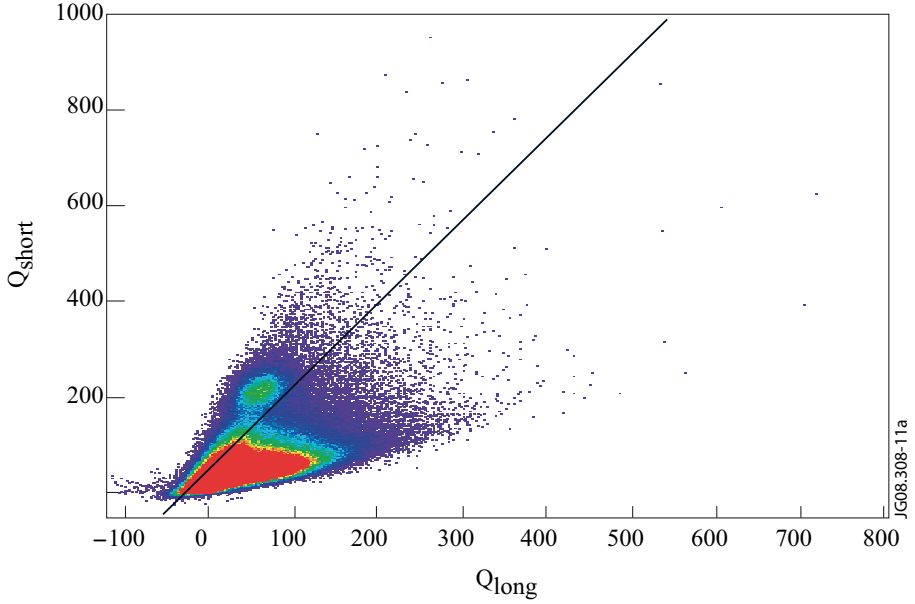


Figure 3.9: The $Q_{\text{long}}, Q_{\text{short}}$ distribution from one hodoscope channel of several hundred JET pulses with the magnet turned on. The proton distribution at $Q_{\text{long}}, Q_{\text{short}}=(70,200)$ is clearly visible. The diagonal line indicates the event selecting cut used here. ©EFDA-JET

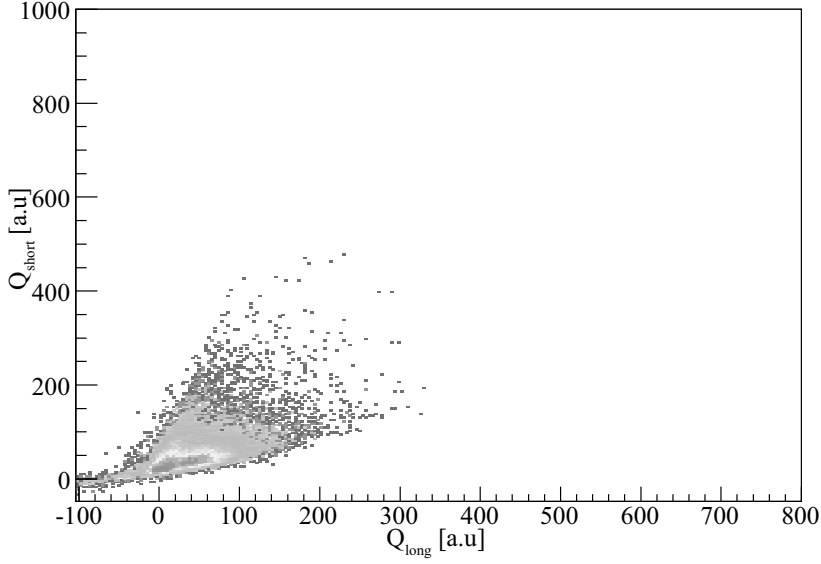


Figure 3.10: The same kind of distribution as in Figure 3.9 but with the magnet turned off.

the magnet turned off, respectively. The operating conditions at JET were the same for both cases. This dataset with the magnet off can be analyzed to provide an estimate of the background situation in the measurements. In the dataset with the magnet on, the proton distribution can clearly be seen in $Q_{\text{long}}, Q_{\text{short}}=(60,200)$, but no such structure is present when the magnet is turned off.

By applying a diagonal cut through the $Q_{\text{long}}, Q_{\text{short}}$ distribution (black line in Figure 3.9) and selecting all events above that cut, we discard a large fraction of the background events. $Q_{\text{tot}} = Q_{\text{long}} + Q_{\text{short}}$ is calculated for the selected events and a traditional pulse-height distribution of Q_{tot} values is constructed (Figure 3.11). A Q_{tot} distribution for the background measurement is obtained in the same way. This $Q_{\text{tot,back}}$ is scaled to the measurement with the magnet turned on in a proton-free region of the Q_{tot} distribution (between blue lines in Figure 3.11) and the difference between the two is calculated. The number of remaining events in a proton region (between green lines in Figure 3.11) is then calculated for each individual phoswich scintillator and interpreted as the number of protons.

3.1.4 Gain correction

The gain factor of a hodoscope channel is the amplification of amplitude of a waveform in the signal chain, such as the amplification in the PSAs and the

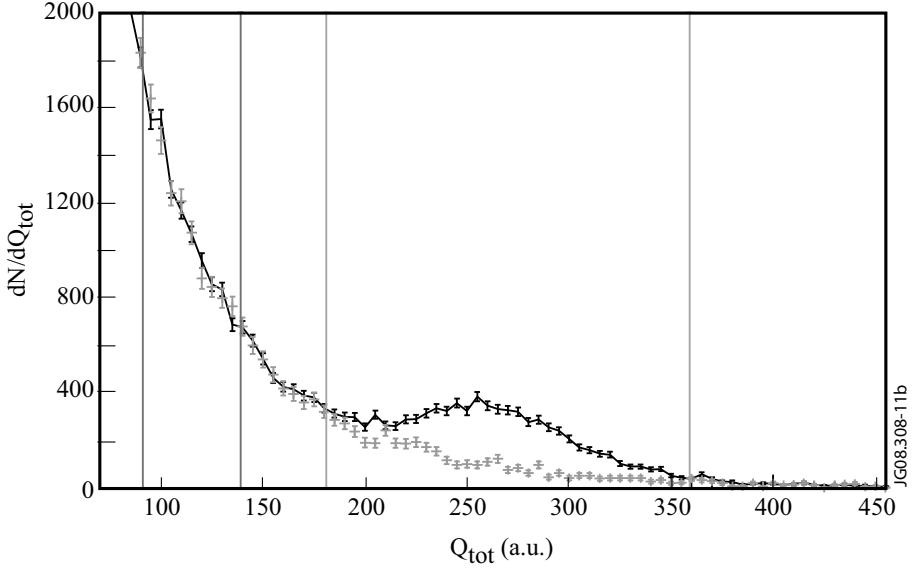


Figure 3.11: Q_{tot} distribution of several hundred summed JET pulses (black dots connected with lines) and the scaled background distribution (red dots). The proton free region is enclosed by two blue vertical lines and the proton region is enclosed by two green vertical lines. ©EFDA-JET

PMTs. A gain factor that varies over time results in a shift of the position of the proton peak in the Q_{tot} distribution. This shift is corrected for by calculating the gain shift of the channels, illustrated in Figure 3.12.

The gain for a hodoscope channel is defined as the ratio between the incoming light on the PMT photo cathode and the collected charge in the TRC. The gain variation (gain shift) of each hodoscope channel for the present dataset, relative to a dataset of a reference JET pulse, is calculated in a four-step algorithm (Paper II):

1. *Determine and correct for the gain shift of the C&M channel:* The average charge of the absolute reference YAP pulses is determined for the present and the reference datasets. The ratio of the two average values is calculated. This ratio is called the gain shift of the C&M channel. The voltage values of all the waveforms of the C&M channel are divided with this ratio to correct for the gain shift.
2. *Determine the variation of the CLS output using the C&M channel:* Using gain shift corrected data from the C&M channel, the average charge of the CLS waveforms are determined for both datasets. The CLS variation ratio, λ , between the two average values is calculated.
3. *Correct for the variation of the CLS output on all other hodoscope channels:* Each CLS waveform of the present dataset of all hodoscope channels are divided by λ to correct for variation of the light intensity of the CLS.

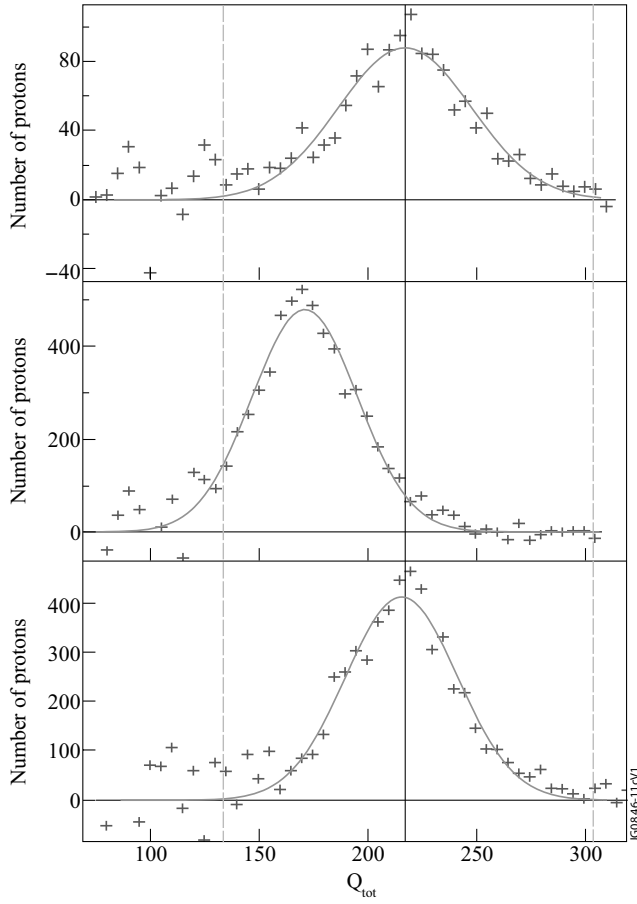


Figure 3.12: Example of the gain correction procedure. All frames show background subtracted Q_{tot} distributions (blue crosses) for a central hodoscope scintillator. The upper frame shows data from JET pulses 68000-68200 and the middle frame non-corrected data from pulses 69000-70100. The lower frame shows the same data as in the middle panel, now corrected for the measured gain shift. See text for details. The red lines are Gaussian fits to the data. The vertical black line is to guide the eye, showing the agreement between the proton distributions in the upper and lower frames. The proton region is indicated by the green dashed vertical lines. ©EFDA-JET

4. *Determine and correct for the gain shift of all other hodoscope channels:* For each hodoscope channel (except the C&M channel), the average charge of the CLS waveform is determined for the present and the reference dataset, using the λ -corrected CLS waveforms for the present dataset. The ratio of the two average values is the gain shift of the hodoscope channel. All waveforms of the present dataset are divided by the determined gain shift, resulting in gain shift corrected waveforms.

In Figure 3.12, an example of the gain shift correction procedure is illustrated. The upper panel shows the Q_{tot} distribution of the gain shift corrected data used as reference from JET pulse 68000-68200. The middle panel shows the uncorrected data from JET pulse 69000-70100. The bottom panel shows the same data as the middle panel, but now gain shift corrected.

After all steps of the data reduction have been performed, the number of remaining events in the pre-defined proton region (see Figures 3.11 and 3.12) is calculated for each individual phoswich scintillator and assembled into a proton position histogram. This histogram constitutes the basis for the further physics analysis of the data.

4. Data interpretation

Neutron spectrometers do not measure neutron energies. The neutron energies must be deconvoluted from the instrument response function (IRF) of the spectrometer. In the continuous case, the Fredholm integral must be solved

$$\xi(x) + \varepsilon(x) = \int IRF(x, E_n) I(E_n) dE_n \quad (4.1)$$

where $\xi(x) + \varepsilon(x)$ is the measured signal ($\xi(x)$ is the true signal and $\varepsilon(x)$ is the noise), $IRF(x, E_n)$ is the instrument response function and $I(E_n)$ is the neutron spectrum. $I(E_n)$ is usually the sought variable. In applied physics, the Fredholm integral is usually used in its discrete form

$$\bar{\xi} + \bar{\varepsilon} = \overline{IRF} \bar{E}_n \quad (4.2)$$

where $\bar{\xi}$ is the instrument response vector, $\bar{\varepsilon}$ is the noise, \overline{IRF} is the instrument response function matrix and \bar{E}_n is the neutron spectrum vector. A naïve approach to solve this problem would be to calculate the (pseudo) inverse of \overline{IRF} , \overline{IRF}^{-1} . We then can write

$$\overline{IRF}^{-1} [\bar{\xi} + \bar{\varepsilon}] = \bar{E}_n. \quad (4.3)$$

In Figure 4.1, an illustration of such a solution is shown. A synthetic Gaussian neutron spectrum (black line in Figure 4.1a) is folded with an IRF of the MPRu resulting in the instrument response. When $\bar{\varepsilon}$ is zero, Equation 4.3 results in the blue dashed line of Figure 4.1. However, if one element of $\bar{\varepsilon}$ is 1% of the corresponding element in $\bar{\xi}$ Equation 4.3 results in the red dotted curve of Figure 4.1. Note that by introducing a *very small* uncertainty in the data the naïve approach is returning unphysical results. Clearly, there is a need of alternative analysis methods.

4.1 Forward convolution method

The forward convolution model solves the Fredholm equation, with the help of parameterised models. The neutron spectrum of a tokamak plasma can be described by superimposed components, the shapes of which are determined by the ion velocity distributions. In the forward convolution method, the mod-

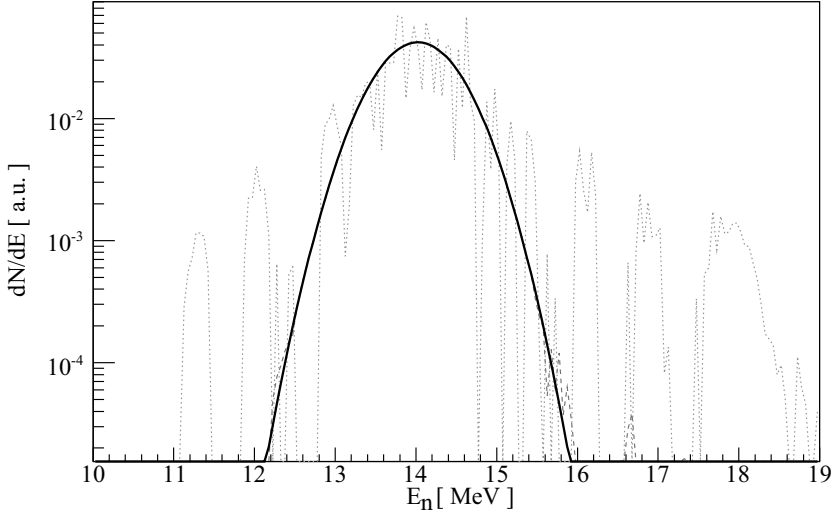


Figure 4.1: Synthetic Gaussian neutron spectrum (black solid) together with the results of Equation 4.3 with $\bar{\varepsilon} = 0$ (blue dashed) and $\bar{\varepsilon} \neq 0$ (red dots).

els are folded with the IRF, which results in modelled instrument spectra. A minimising routine is then used to minimise χ^2 or C using the parameters of the models as free variables.

$$\chi^2 = \sum_i \frac{(x_i - m_i)^2}{\sigma_i^2}, \quad (4.4)$$

where x_i and m_i are the data and the modelled instrument spectra, respectively, and σ_i is the uncertainty of the data in the i :th bin. χ^2 should be used in the case of Gaussian statistics. For Poisson statistics C should be used [41], which is defined as

$$C = -2 \sum_i x_i \ln(m_i) - m_i - \ln(x_i!). \quad (4.5)$$

The following subsections illustrate some different analysis where the forward convolution method has been applied.

4.1.1 Magnetic proton recoil spectrometer data

4.1.1.1 Statistical uncertainty estimation

In Figure 4.2, the MPRu data of JET pulse 68569 is shown. The plasma was in this case heated with NBI only and, consequently, the ions belong either to a thermal or a NBI slowing down population. Here we use this data to

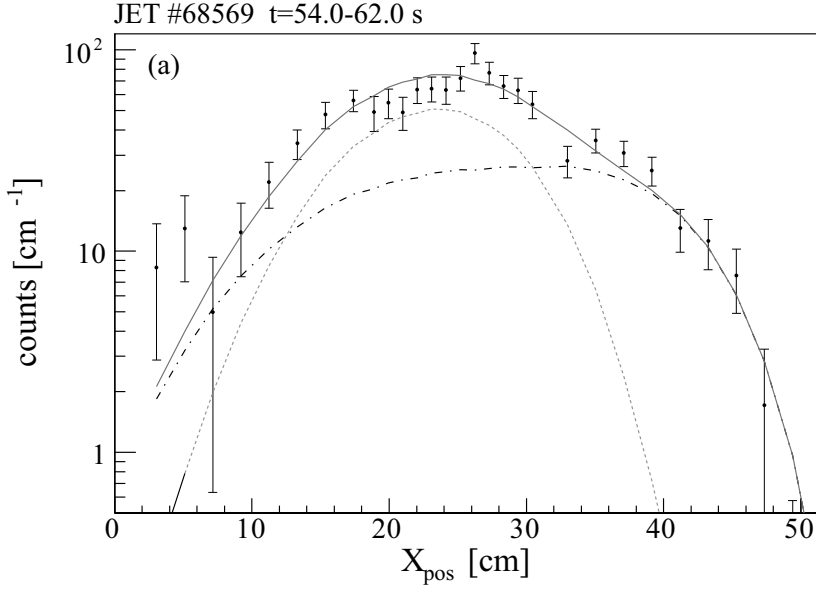


Figure 4.2: Experimental proton position histogram of the MPRu (points with error bars) from JET pulse 68569 together with the fitted and folded components due to NBI-thermal (black dash dotted) and thermal-thermal (red dashed) interactions as well as their sum (blue solid).

illustrate the uncertainty estimation technique available through the forward convolution method.

Two components are used in the forward convolution fit to the MPRu data of JET pulse 68569; a thermal-thermal and a thermal-NBI neutron component, shown in Figure 4.3. The free parameters used in the minimisation routine of the forward convolution method are the intensities of the two components (I_{thermal} , I_{NBI}) and the energy shift (dE) of the thermal-thermal component.

The energy shifts, dE , of the thermal-NBI and the thermal-thermal components corresponds to a motion of either one or both of the two reacting ion populations relative to the observer, this is due to the third term of Equation 2.5. This term is the only one sensitive to the sign of the toroidal rotation. The NBI ions of the slowing down distribution are not affected by the plasma rotation until they are thermalised. A detailed calculation of this situation [42] gives as a result that the shift of the thermal-NBI component is set to half of the shift of the thermal-thermal component.

The statistics of the data in Figure 4.2 does not allow for a free fit of the temperature of the thermal-thermal component. Instead, this temperature is set to 5 keV as measured by charge exchange recombination spectroscopy (CXRS).

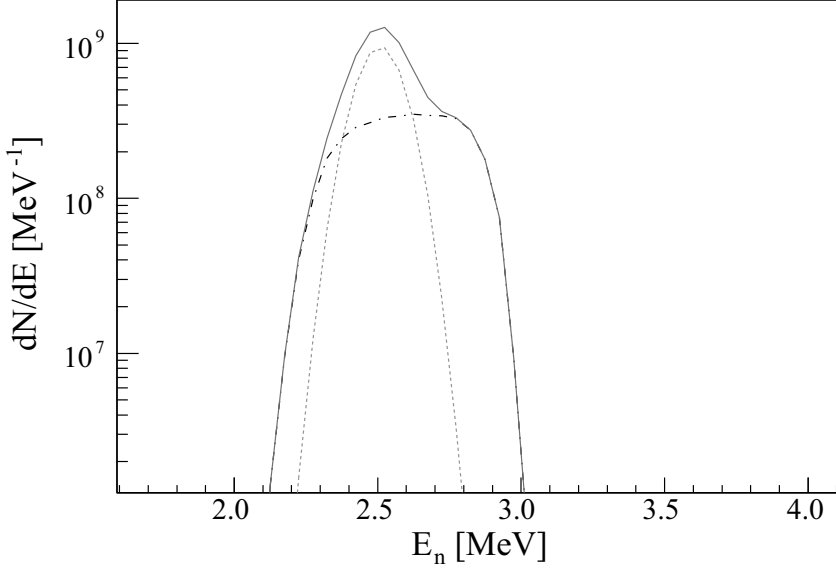


Figure 4.3: The best fit neutron energy components of the thermal-NBI (black dash dotted), the thermal-thermal (red dashed) and their sum (blue solid), giving the folded result in Figure 4.2.

The intensity ratio between thermal and non-thermal (here, NBI) components (the thermal fraction, $R_{\text{th}} = I_{\text{thermal}}/(I_{\text{thermal}} + I_{\text{NBI}})$) is an important performance indicator for a fusion reactor. Ideally, a fusion reactor should be self-sustained driven only by internal thermal reactions; this is the burning plasma condition discussed in Section 1.1. Thus, in an ideal thermonuclear reactor R should approach one.

The reduced χ^2 , i.e. χ^2 per degree of freedom, of the fit is 1.24. The (integrated) intensities of the thermal-thermal and the thermal-NBI components are $I_{\text{thermal}} = (135 \pm 17) \cdot 10^6$ (neutrons) and $I_{\text{NBI}} = (250 \pm 19) \cdot 10^6$ (neutrons), respectively. The intensities given here are the estimated number of neutrons impinging on the target foil. The best fit intensities give a thermal fraction of $R_{\text{th}} = 0.35 \pm 0.05$. The energy shifts for the thermal-NBI and thermal-thermal components are $dE_{\text{NBI}} = 18 \pm 4$ keV and $dE_{\text{thermal}} = 36 \pm 8$ keV, respectively, corresponding to a plasma rotation of 229 ± 51 km/s for the thermal ion population, according to Equation 2.9. This value can be compared to the plasma rotation in the plasma core as measured by CXRS diagnostics of about 170 km/s with a systematic uncertainty of 5%-10%.

A full map of χ^2 as function of the two component intensities ($I_{\text{NBI}}, I_{\text{thermal}}$) is shown in Figure 4.4, where the temperature of the thermal component and the energy shifts of both components are kept constant. As can be seen, the intensities of the two components are anti-correlated. The correlation contour

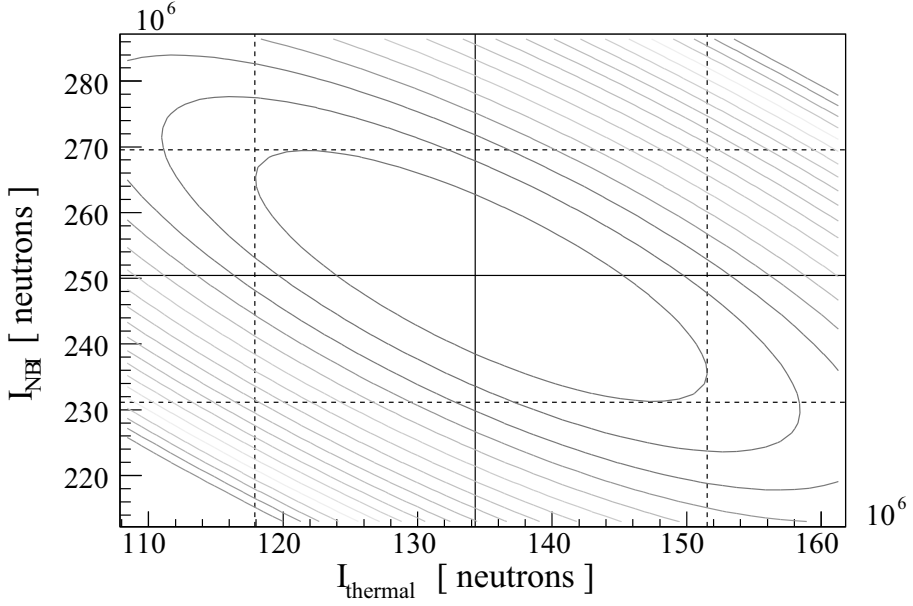


Figure 4.4: Contour map of χ^2 as a function of the intensities of the thermal-thermal and NBI-thermal components. Each contour level indicates an increase in χ^2 of one unit (+1) from its minimum value χ^2_{\min} found at $I_{\text{NB}} = 250 \cdot 10^6$ (neutrons), $I_{\text{thermal}} = 135 \cdot 10^6$, as indicated by the full vertical and horizontal lines. The parameter values corresponding to a one-sigma interval ($\chi^2_{\min} + 1$) are indicated with vertical and horizontal dashed lines.

map in Figure 4.4 is used to estimate the (one-sigma) uncertainties of the intensities (indicated by the dashed lines).

4.1.1.2 Tritium burn up

In a D plasma, tritium is produced through reaction 2 in Table 1.1. This tritium reacts with the bulk plasma and produces 14-MeV neutrons. The MPRu can clearly see a 14-MeV neutron contribution when set to 14-MeV measurements of D plasmas. In Figure 4.5, the proton position histogram measured by the MPRu when set to 14-MeV measurements for about 230 summed JET discharges is shown. Besides the tritium burn-up neutrons (TBNs), a clear contribution from the residual tritium with $I_{\text{residual}}/I_{\text{tot}} = 9\%$ can be seen as well, which is agreement with previous results [43]. The free parameters of the forward convolution fit are the intensities of the components.

4.1.1.3 Third harmonic heating

JET discharge 74951 was one of the record shots of JET, in terms of DD neutron production per applied heating power. The discharge had 3 MW of NBI heating and 3 MW of 3rd harmonic deuterium ICRH applied with a res-

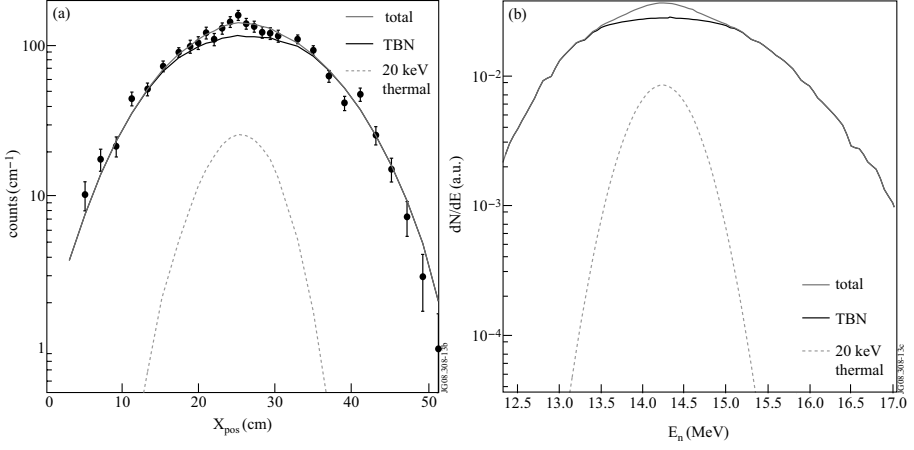


Figure 4.5: (a) TBN measurement of 230 summed JET discharges of the MPRu, together with a TBN (black) and residual (red dashed) component folded with the IRF and fitted to the data. (b) The fitted TBN (black) and residual (red dashed) components as a function of E_n

onance layer at R_{major} equals 3 m. This discharge has been extensively studied in terms of neutron energy spectrometry. In [44] an unfolding procedure is presented, which calculates the ion energy distribution from TOFOR data (Figure 4.6a) by fitting ICRH components to the TOFOR data using an iterative method. TOFOR [35] is a TOF spectrometer, which has a radial LOS to the JET plasma, i.e. 90° to the magnetic field. The response of TOFOR to 2.5-MeV neutrons is peaked around $t_{\text{TOF}} = 65$ ns. Here the TOFOR data from 60 ns and below are used in the unfolding. It should be noted that the unfolded ion energy distribution translated to the ICRH+NBI component (blue) in Figure 4.6a fits the high-energy part of the TOFOR data, i.e. below 60 ns, quite well. However, for the low energy part above 60 ns the component differs considerably from the data. This can be explained as follows: the position of the resonance layer of the ICRH is positioned just outside the LOS of TOFOR (blue rectangle in Figure 4.7). The turning point of the ICRH accelerated ions will have a guiding centre at the resonance layer which is on the border to the LOS edge of TOFOR. As can be seen in Figure 4.7, where a 2 MeV deuterium orbit is shown (black line), the fraction of ions moving towards TOFOR during the cyclotron motion compared to those moving away will be higher than the unfolding technique suggests due to the Larmor radius of the ions.

The unfolded ion energy distribution (Figure 4.6b), obtained from the TOFOR data, has been used to calculate the neutron energy spectrum related to the LOS of the MPRu (Figure 4.6c). Using CONTROLROOM, we calculate the neutron emission spectra in the viewing angle 47° to the magnetic field, i.e. the MPRu LOS (red rectangle in Figure 4.7). The ratio v_\perp/v was assumed to be close to 1, which is an appropriate approximation since the ICRH ac-

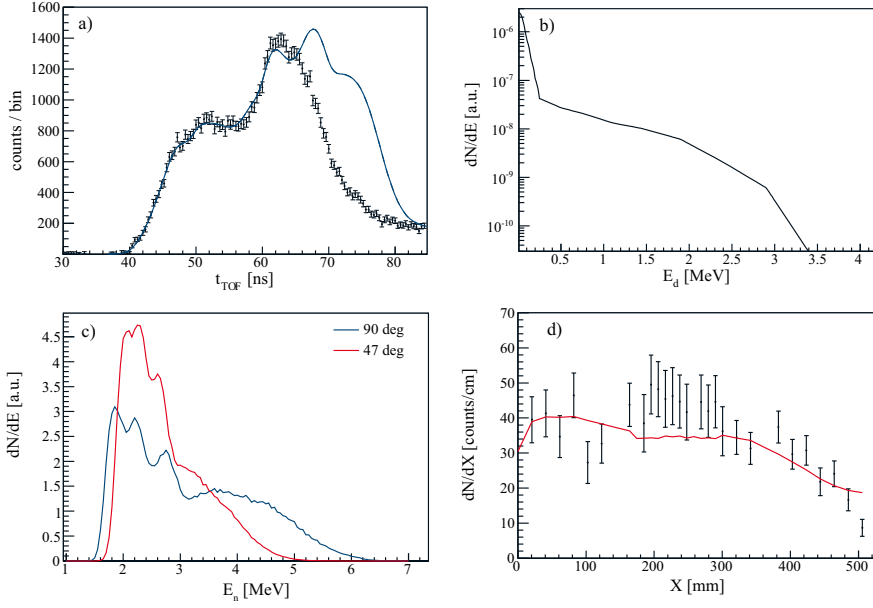


Figure 4.6: a) TOFOR data from JET discharge 74951 (dots with error bars) together with folded result of the unfolding procedure in [44] (blue line). b) Energy distribution obtained from with the unfolding procedure described in [44] from TOFOR data. c) Neutron energy spectrum of 3rd harmonic heating component calculated from TOFOR data in a LOS perpendicular (blue line) and with 47° to the magnetic field. d) MPRu data from JET discharge 74951 (dots with error bars) together with folded and fitted neutron spectrum in c.

celerates ions in the perpendicular direction to the magnetic field. We expect the neutron energy spectrum to fit the MPRu data, even at low energies, since the MPRu has a tangential LOS and consequently no Larmor radius effects, such as those discussed in the TOFOR data case, are expected. The calculated neutron energy spectrum is folded and fitted to the MPRu data using only the intensity as free parameter for the forward convolution method. In Figure 4.6c, the folded and fitted component is shown (red line) together with the MPRu data (dots). The reduced χ^2 of the fit is 1.8.

This rather good fit is interesting since it experimentally confirms the unfolding method of [44], even if somewhat anecdotally. Furthermore, the hypothesis of the influence of the Larmor radius on the neutron spectrum seen by TOFOR is supported, since the low energy part ($X_{\text{pos}} < 100$ mm) of the calculated MPRu component fits to the data.

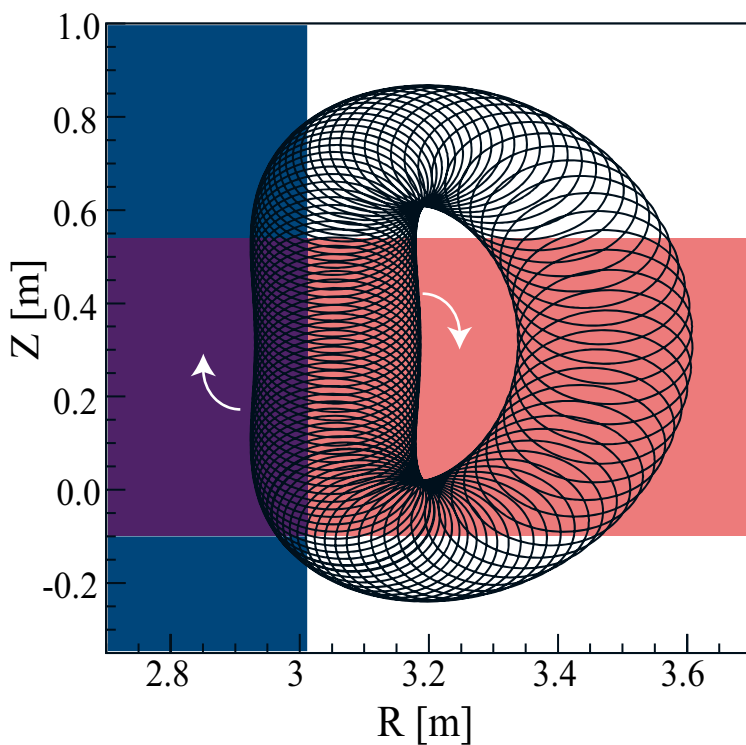


Figure 4.7: A 2 MeV deuterium orbit (black line) is shown together with the lines of sight of TOFOR (blue) and MPRu (red).

4.1.2 Fusion power measurements of deuterium plasmas using a neutron camera-spectrometer system

The MP Ru is *ab initio* calibrated, i.e. the flux on the foil of the spectrometer can be estimated from basic physical parameters. In [45] this *ab initio* calibration has been used, together with the neutron camera discussed in Section 2.1.3, to measure the absolute neutron yield of DT plasmas. In this section, the initial work with this method on DD plasmas is presented.

The neutron emission profile is estimated from the data of the neutron camera. The standard magnetic equilibrium code `EFIT` [46, 47] is used to get the normalised minor radius, ρ . The neutron emission profile, Γ , is modelled as being constant on a flux surface, using either a Gaussian or a peaked profile function:

$$\Gamma_G(\rho|A_{\text{fit}}, \sigma_{\text{fit}}) = A_{\text{fit}} e^{-\frac{\rho^2}{2\sigma_{\text{fit}}^2}} \quad (4.6)$$

or

$$\Gamma_P(\rho|A_{\text{fit}}, \alpha_{\text{fit}}) = A_{\text{fit}}(1 - \rho^2)^{\alpha_{\text{fit}}} \quad (4.7)$$

where A_{fit} is the intensity of the emission, σ is the spread of the Gaussian component and α_{fit} is the peaking factor.

The optical detector response to the emission profile is calculated by `LINE1`. The `LINE1` code uses an optical model where JET structures are either opaque or transparent. `LINE1` splits the volume inside the vacuum vessel into voxels and calculates the solid angle seen by a detector from each voxel. In Figure 4.9, the LOS matrices of the 19 neutron camera channels and the MP Ru at JET are shown obtained by `LINE1`. The colour intensities in the figure corresponds to the fractional solid angles (projected on a poloidal plane) that the corresponding detector sees from that voxel. Γ is folded with the LOS matrices to calculate the modelled neutron flux at the camera detectors, $F_{\text{camera,calc}}$, and at the MP Ru foil, $F_{\text{MP Ru,calc}}$.

$$F_n = \sum_i \sum_j \overline{LOS(R_i, Z_j)} \Gamma(R_i, Z_j) \quad (4.8)$$

where $\overline{LOS(R_i, Z_j)}$ is the LOS matrixes of one of the two detector systems. The forward convolution method is used to fit the parameters of Γ to the data of the neutron camera, minimising χ^2 .

Due to the *ab initio* calibration of the MP Ru, the flux at the foil, $F_{n,\text{meas}}$, of the spectrometer can be calculated from the measured proton histogram. However, to relate the measured neutron flux on the MP Ru foil to that of the optical model described above we must correct the measurement for non-optical effects. Such correction factors are shown in Table 4.1. The attenuation, transmission and the two scattering corrections have been estimated using two `MCNPX` [48] models; one modelling the machine effects (attenua-

Table 4.1: *Correction factors for yield method*

Factor	Abbreviation	Value
Attenuation	C_{att}	0.78
Transmission	C_{tr}	1.15
Scatter machine	C_{sm}	1.02
Scatter collimator	C_{sc}	1.01
Anisotropy	C_{an}	0.98
Thermal insulation	C_{th}	0.99

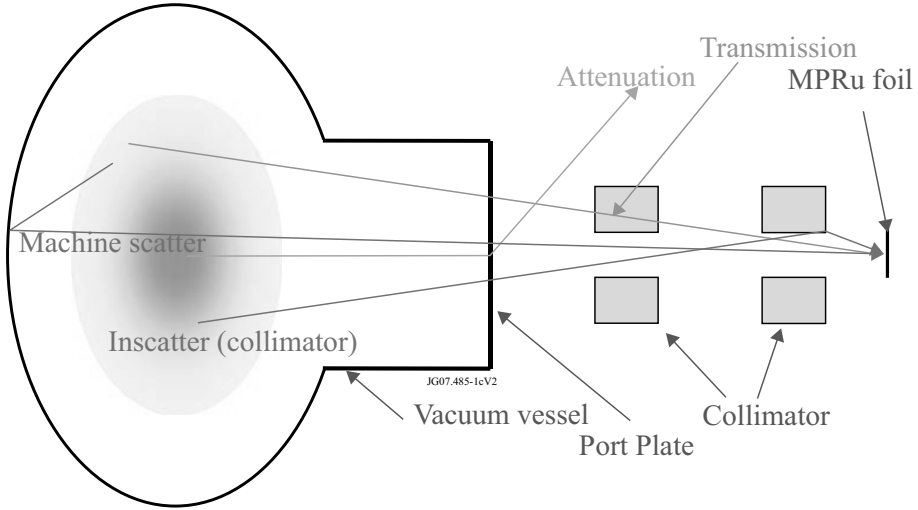


Figure 4.8: Schematic drawing of the vessel of JET and the collimation of the MPRu together with the effects

tion, transmission and machine scattering) and one the collimator scattering. The processes involved in the scattering related fluxes are illustrated in Figure 4.8. Note that the effect of the thermal insulation is not part of the MCNPX attenuation calculation but treated separately.

In the DT yield determination [45], no correction for anisotropy was deemed necessary (i.e. $C_{an}^{14} = 1.0$) due to the isotropic cross section of the DT reaction. In the DD case, however, the cross section is highly peaked in the forward and backward directions. The anisotropy correction, C_{an} , has been estimated from TRANSP [49] simulations, using thermal as well as beam heated and suprathermal plasmas as input.

With the correction factors, the intensity of the neutron emission profile is renormalized and corrected as

$$A_{MPRu} = A_{fit} \frac{F_{MPRu, meas}}{F_{MPRu, calc} \prod_i (C_i)}, \quad (4.9)$$

where C_i corresponds to the correction factors in Table 4.1. Finally the neutron yield, Y_n can be calculated as the sum over the neutron yield in each voxel

$$Y_n = \sum_j \sum_i \Gamma(\rho(R_i, Z_j) | A_{MPRu}, \sigma_{fit}) R_i \Delta R_i \Delta Z_j, \quad (4.10)$$

where (R_i, Z_j) is the centre of the voxel and ΔR_i and ΔZ_j are the widths and heights of the voxels. In Figure 4.10, the neutron yield from this method (Gaussian (blue) and peaked emissivity model (red)) is plotted versus the cross-calibrated fission chamber measurements. In Figure 4.11, the χ^2 distribution of the Gaussian (blue) and peak (red) fit to camera data is shown. We can clearly see that for a majority of the pulses the Gaussian distribution is not an appropriate model of the neutron emission profile. The extra peak of the Gaussian χ^2_{red} distribution around 6 can be interpreted in (at least) two ways: either we dismiss the Gaussian model as non-suitable or we interpret this peak as a missing fitting component to the camera data. Recently, a parameterisation of $\Gamma(R, Z)$ has been developed [50]. This parameterisation is planned to be used in future work to be able to analyse, e.g. beam-dominated plasmas. The inclusion of such components might improve the χ^2_{red} distribution of the Gaussian fit.

All JET discharges which give a $\chi^2_{red} < 3$ in the model fit to the camera data are selected and shown in Figure 4.10. A linear fit to the two datasets gives

$$Y_{MPRu, Peak} = 1.052(\pm 0.002) Y_{FC} \quad (4.11)$$

and

$$Y_{MPRu, Gauss} = 1.077(\pm 0.004) Y_{FC} \quad (4.12)$$

4.2 Unfolding methods

Several unfolding techniques have been developed and used to unfold data. In neutron emission spectrometry, the most commonly used methods are the Thikonov regularisation [51], maximum entropy [52] and minimum Fisher regularisation (MFR) [53]. Unfolding methods are usually using each bin of \bar{E}_n as a free parameter and try to maximize or minimize a quantity, adding some constraints to the calculations of \bar{E}_n . Such constraints can be non-negative values or a smoothness level in \bar{E}_n . Paper IV is devoted to evaluating some of these unfolding techniques commonly used in Neutron Emission Spectroscopy.

MAXED [52], short for MAXimum Entropy Deconvolution, is one of the most commonly used unfolding codes for neutron spectrometry at JET. MAXED is based on information theory to find the most probable neutron spectrum, given the measured data, the IRF, a target χ^2 and an a

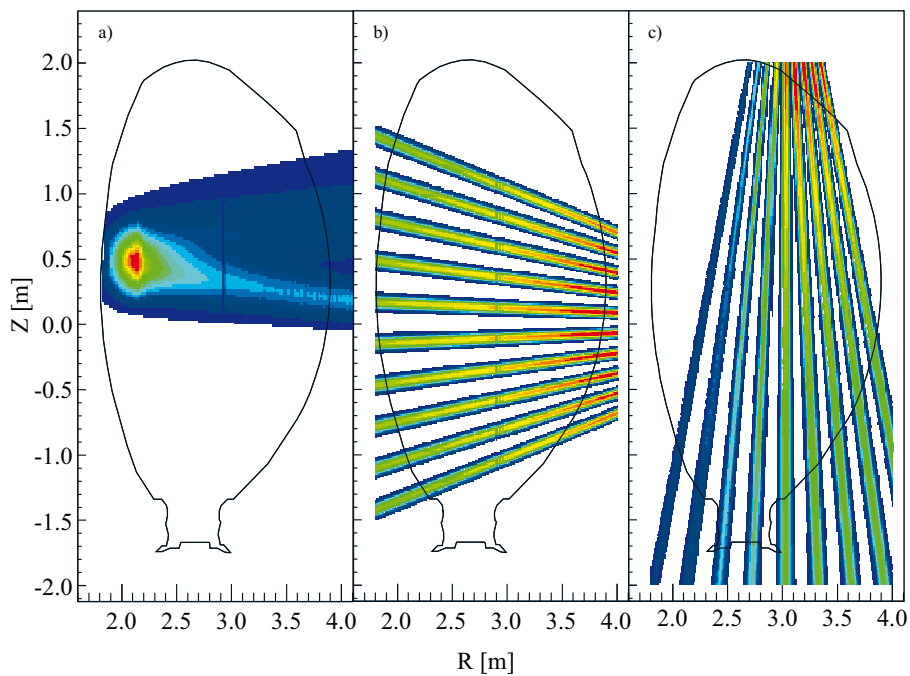


Figure 4.9: Projected LOSs on the poloidal plane of (a) the MPRu, (b) the horizontal and (c) the vertical camera.

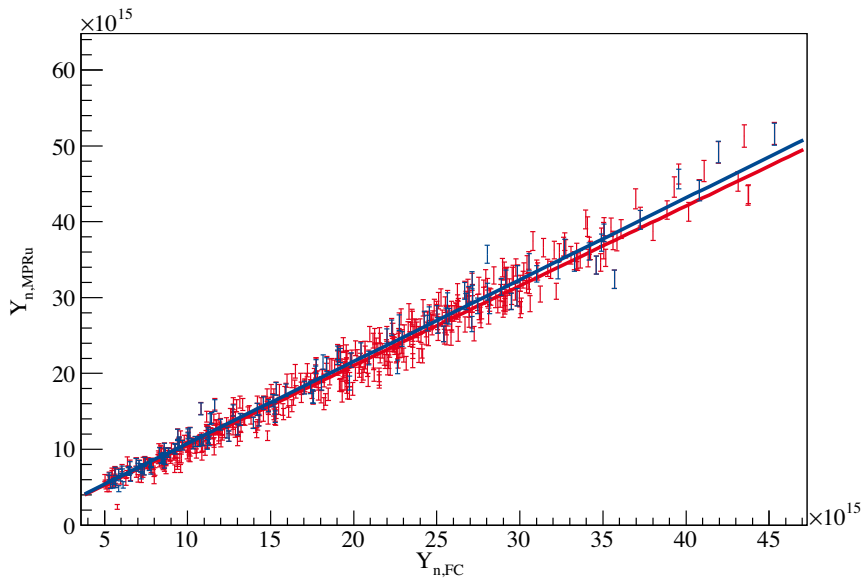


Figure 4.10: Neutron yield measured with the MPRu-camera system vs. fission chamber in the JET discharge region 68000 - 73700 using a Gaussian(blue) and peaked (red) function together with the fitted curves described by Equation 4.12 and 4.11. The error bars are the statistical uncertainties of the MPRu.

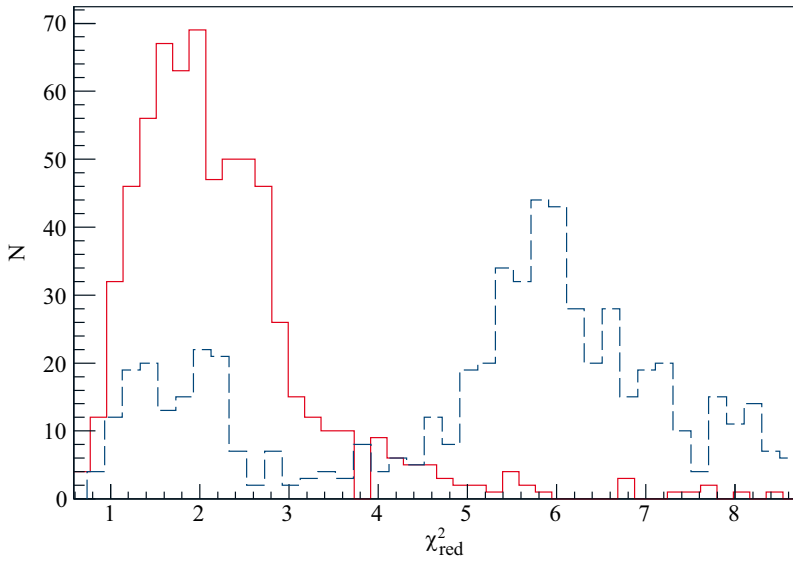


Figure 4.11: χ^2_{red} distribution of Gaussian (blue dashed) and peak (red) function fit to camera data in the JET discharge region 68000 - 73700.

priori spectrum. All prior knowledge about the problem can be included in the *a priori* spectrum. A common approach is to give a uniform *a priori* spectrum, which implies no assumed knowledge about the problem. Bayesian analysis methods based on models describing the data, similar to the forward convolution method described in this thesis, has been suggested to give reliable *a priori* information[54].

One problem of MAXED is the choice of target χ^2 , χ_{target}^2 . The average of a χ^2 distribution equals the number of free variables in the problem, i.e. the number of bins in the measurement. However, this is only the *average* of χ^2 , and, consequently, it is hard to know what χ_{target}^2 to use. In fact, this is a common problem for many unfolding techniques. In Tikhonov regularisation and in MFR, a regularisation parameter must be chosen and this influences the solution in a similar way as χ_{target}^2 . One suggested solution to this problem is the so called L-curve solution [55].

MAXED has been applied to the real experimental data of pulse 68569 using a Gaussian starting spectrum. This pulse is the same as was used in Section 4.1.1.1 to illustrate the uncertainty estimation of the forward convolution method. Before unfolding the data, the *a priori* spectrum is selected by a Gaussian fit to the data, using the forward convolution method described above. In Figure 4.12, the calculated neutron energy spectrum using MAXED is shown (red curve) together with the summed components of the forward convolution method analysis (black curve), from Section 4.1.1.1. In Figure 4.13, the proton position histogram is shown (points with error bars) together with the folded (and summed) components of the forward convolution method (blue) and the folded MAXED neutron spectrum (red). The shape of the MAXED spectrum closely resembles the shape of the estimated neutron spectrum of the forward convolution method (red). This gives some confidence that the performed analysis is correct, in particular regarding the NBI model used in the forward convolution analysis.

In Section 4.3.2 (and Paper IV), an evaluation of MAXED is presented using synthetic data.

4.3 Evaluation procedure using synthetic data

In Paper IV and VI, an evaluation method has been used to assess the performance of unfolding codes and the time resolution of neutron spectrometers at ITER. In both evaluations, a synthetic neutron energy spectrum, \bar{I}_n , is created and folded with an IRF (Equation 4.2). This folding results in an ideal synthetic measurement, $\bar{\xi}_{ideal}$. A Poisson fluctuation is added to each bin of $\bar{\xi}_{ideal}$, resulting in a synthetic measurement, $\bar{\xi}_{meas}$. The properties of \bar{I}_n is reconstructed from $\bar{\xi}_{meas}$ using either an unfolding code (as in Paper IV) or the forward convolution method (as in Paper VI). In Figure 4.14, \bar{I}_n (blue) for a thermal neutron spectrum is shown together with $\bar{\xi}_{ideal}$ (red) and $\bar{\xi}_{meas}$

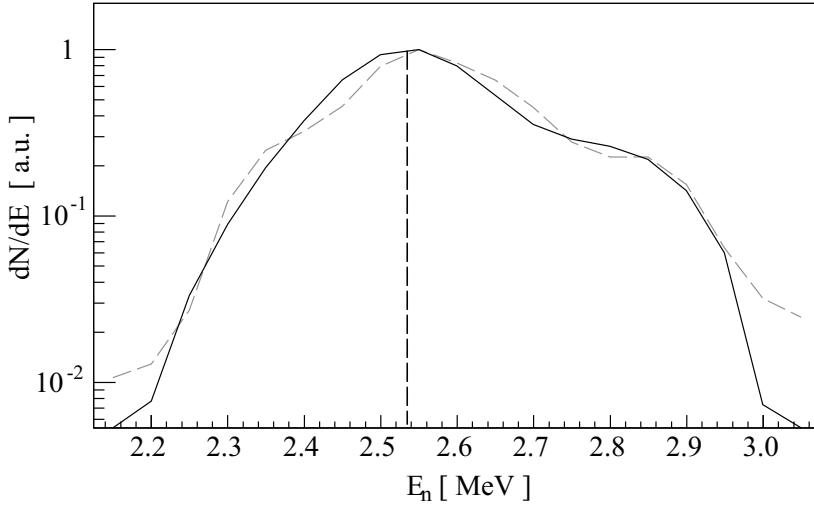


Figure 4.12: Calculated neutron energy spectrum from forward component fitting (black) and MAXED unfolding (red dashed). The black dashed line indicates the centre of the thermal-thermal component of the forward convolution analysis.

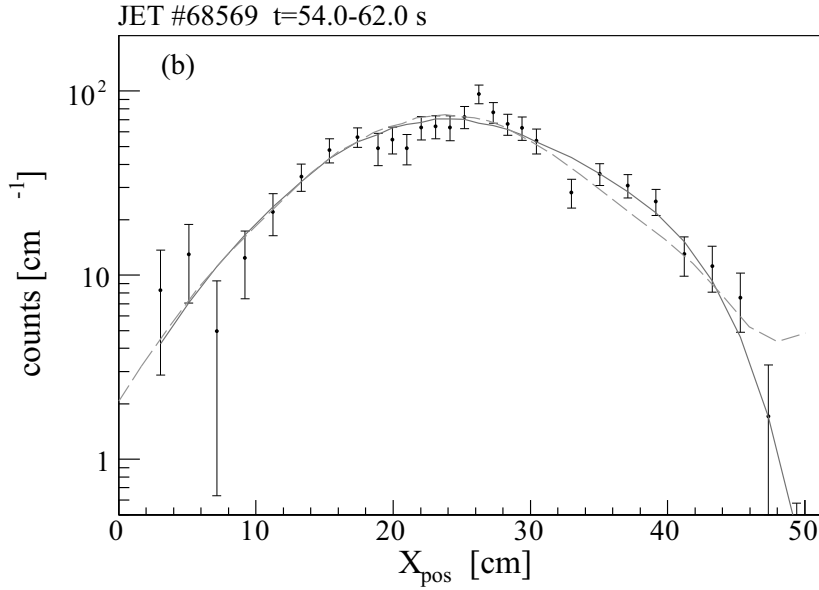


Figure 4.13: Proton position histogram of NBI heated JET discharge 68569 as measured by the MPRu (points with error bars) and the two neutron energy spectra from Figure 4.12 folded with the IRF; from the forward component fitting (black) and from MAXED unfolding (red dashed).

(crosses) for a organic scintillator. The evaluation procedure is repeated with the same neutron spectrum to estimate the influence of statistics. An overview of the evaluation method is shown in Figure 4.15.

4.3.1 Evaluation of instrument response functions

Presently, a high resolution neutron spectrometer (HRNS) at ITER, such as those discussed in this thesis, is “enabled”. In the case of HRNS, this means that there is a dedicated LOS and position. However, there is a pending decision on what type of spectrometer that should be installed, if any, and who should be financially responsible for it.

In Paper VI, five different neutron spectrometer techniques are evaluated in terms of time resolution, using synthetic data obtained from ITER like plasma conditions [56, 57]. The requested time resolution, Δt , for temperature measurements at ITER is 100 ms with a precision of 10% [19]. The neutron flux, $1 \cdot 10^9 \text{ n/cm}^2/\text{s}$ for a first wall aperture of 50 mm radius and $T_i=20 \text{ keV}$, and neutron energy distributions are calculated with the LOS and position dedicated to the HRNS for a 500 MW plasma. The five evaluated neutron spectrometer techniques are: MPR, TPR, TOF, diamond and gamma discriminating organic scintillators (GDOSs).

In the thermal case, the ion temperature is varied from $T_i=1$ to 40 keV in steps of 2 keV and the neutron flux is scaled according to the change in reactivity (Figure 1.1). For each temperature the integration time, Δt , is varied. For each combination of Δt and T_i , the precision and accuracy is calculated. In Figure 4.16, the precision as a function of Δt and T_i is illustrated for the MPR technique. The precision improves from the lower left to the upper right of the figure. The red line in the figure corresponds to the 10% precision line. This 10% precision line has been calculated for all five spectrometer techniques in the same way and are shown in Figure 4.17. It is clear from this evaluation that the thin-foil techniques (MPR and TPR) have better time-resolution than the other techniques for measurements of T_i .

4.3.2 Evaluation of unfolding techniques

In Paper IV, the performance of several unfolding techniques is evaluated. Here we focus on MAXED and give some examples of results of the evaluation procedure. The unfolding techniques generate neutron spectra from the measured data, using the IRFs of the measurement. The output of the evaluation procedure is consequently a set of neutron spectra, \bar{I}_{unf} . To quantify the performance of the unfolding techniques, the metric q was introduced

$$q = \frac{\sum_{i=1}^n |I_{\text{unf},i} - I_{n,i}|}{\sum_{i=1}^n I_{n,i}}, \quad (4.13)$$

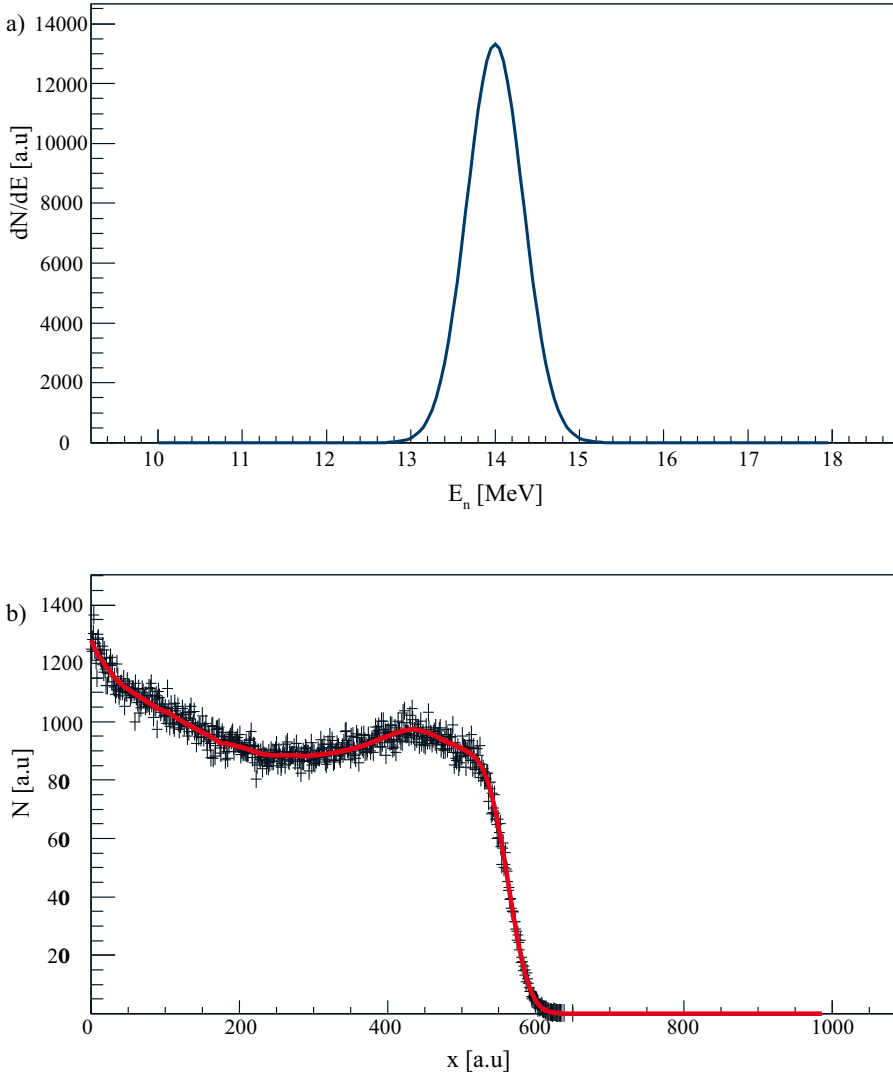


Figure 4.14: (a) Synthetic neutron spectrum from a plasma in thermal equilibrium. (b) Ideal measurement, ξ_{ideal} (red), together with synthetic measurement, ξ_{meas} (crosses), of a technique with an IRF of an organic scintillator.

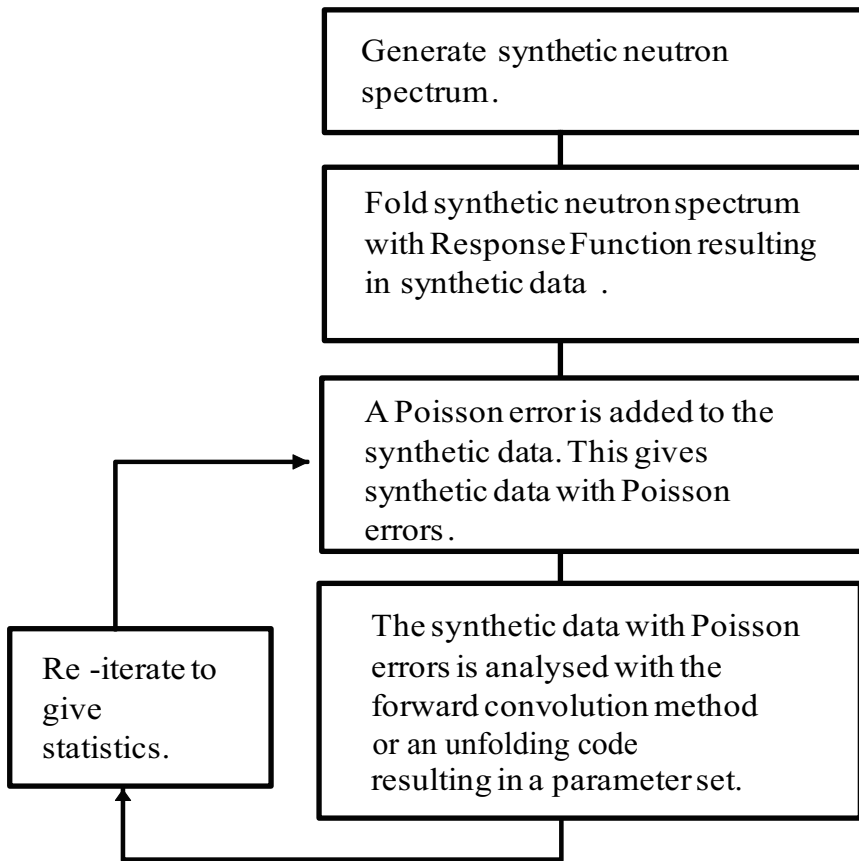


Figure 4.15: Overview of the evaluation procedure.

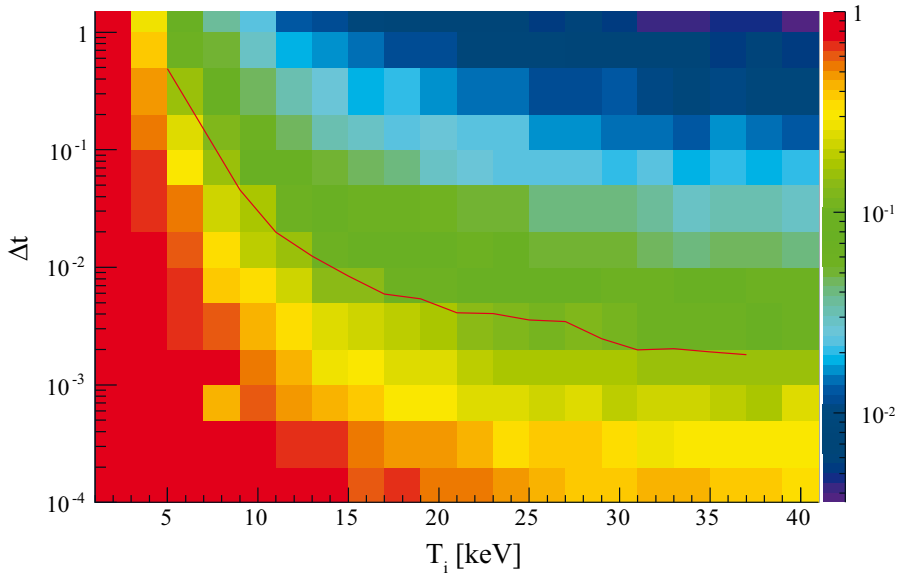


Figure 4.16: The precision of T_i as a function of T_i and Δt for the MPRu technique.

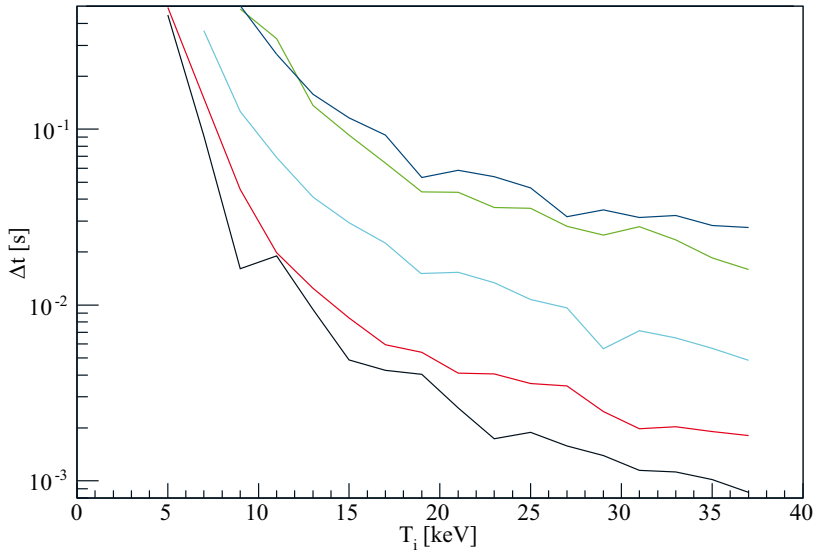


Figure 4.17: The 10% precision lines of the TPR (black), MPR (red), TOF (turquoise), GDOS (green) and diamond (blue) techniques.

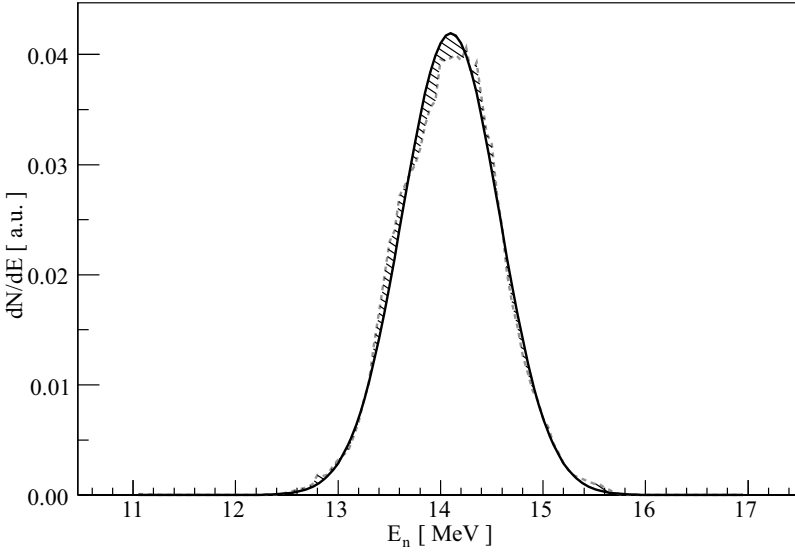


Figure 4.18: Initial synthetic (thermal) neutron spectrum (black solid line) and unfolded neutron spectrum (red dashed line) from a folding-unfolding process using MAXED, as described in the text. The shaded area between the two spectra corresponds to the q metric.

where n is the number of bins in the neutron spectra. Note that q is zero when the unfolded spectrum is identical to the synthetic spectrum. The metric q is represented by the shaded area in Figure 4.18, where a synthetic thermal neutron spectrum (black) is shown together with an unfolded spectrum (from MAXED), obtained with a target $\chi^2=1$ and a flat *a priori* information.

The evaluation procedure has been repeated 100 times with different number of counts, N , in $\bar{\xi}_{\text{ideal}}$, where $\bar{\xi}_{\text{ideal}}$ is a thermal neutron spectrum ($T_i=20$ keV) and for two IRFs: the MPRu and one for organic scintillators (NE213). The result of this study is shown in Figure 4.19, where the average value of q , $\langle q \rangle$, of the MPRu (black) and the NE213 (red) is shown. The MPRu would reach a $\langle q \rangle$ of 10% when $N=4 \cdot 10^4$ and NE213 when $N=10^6$. Comparing to the ITER like conditions in Section 4.3.1, we can assume a maximum count rate of 1 MHz for the organic scintillator, which would imply a possible neutron energy spectrum reconstruction with a q of 10% with a time resolution of 1 s. Continuing the comparison to Section 4.3.1, assuming a neutron flux of $1 \cdot 10^9 \text{ n/cm}^2$, the MPRu would have a time resolution of 0.8 s.

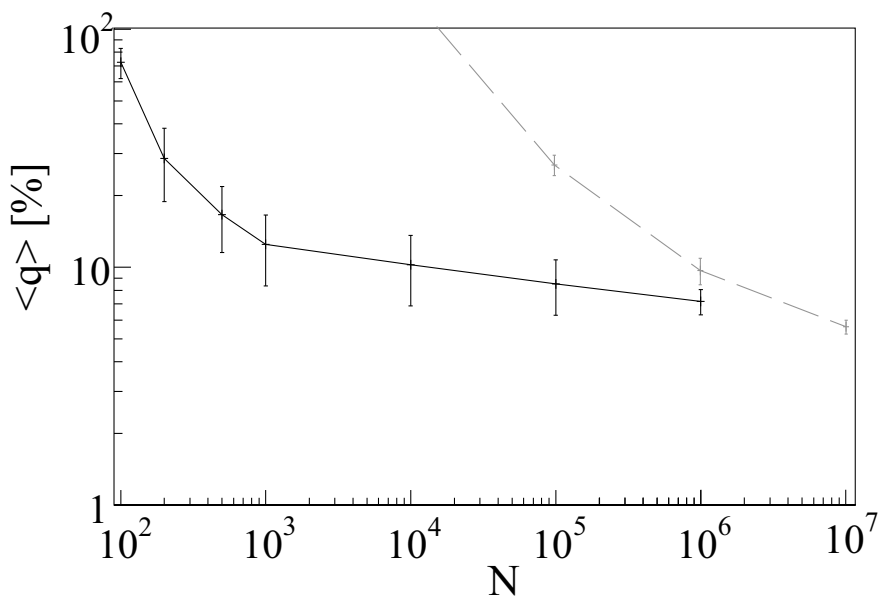


Figure 4.19: $\langle q \rangle$ as a function of number of counts for MPR (black) and NE213 (red) using MAXED. The error bars indicate the standard deviation of the q distribution.

5. Conclusions

In this thesis, neutron spectrometry has been reviewed as a tool for obtaining relevant fusion plasma parameters such as ion temperature, fusion power and $Q_{\text{thermal}}/Q_{\text{tot}}$. It has been illustrated that neutron spectrometers is capable of determine plasma parameters from both 2.5 and 14 MeV neutrons.

The work of this thesis has resulted in the upgrade of the MPR, which has reduced the background sensitivity and, consequently, allowed for D plasma measurements. Furthermore, the data reduction and control and monitoring system have been developed and refined.

MPRu data have been investigated for plasma heating scenarios at JET, such as 3rd harmonic ICRH and NBI heating. Furthermore, the tritium burn up neutrons have been measured together with the neutrons emitted from residual tritium reactions with the bulk plasma. In addition, a novel neutron yield measurement technique for D plasmas is presented. This technique is based on the use of a high resolution neutron spectrometer together with the neutron emission profile, which is measured with a neutron camera. A necessity for this technique to work is a well characterised LOS as well as an *ab initio* or *in situ* calibration of the neutron spectrometer.

Several unfolding techniques have been investigated with the help of synthetic data to estimate the performance of the codes. Furthermore, one of the codes, MAXED, has been applied to data from NBI heated plasmas.

Finally, the time resolutions of five different neutron spectrometry techniques for 14 MeV measurements at ITER have been investigated using synthetic data. The study concludes that the thin-foil spectrometers have the best time resolution of the investigated techniques.

6. Summary in swedish

Vetenskapsmän har i mer än 50 år försökt att tämja solens källa till energi: kärnfusion. Kärnfusion är när två lätta atomkärnor slås samman, fusionerar, och energi frigörs. Denna energi frigörs på grund av att det nya masstillståndet efter reaktionen är lättare än vad de två lättare atomkärnorna var tillsammans. Skillnaden i massa före och efter reaktionen ger den frigjorda energin, enligt Einsteins berömda formel $E = mc^2$.

En av de mest lovande kärnreaktionerna för fusion, i energiproduktionssammanhang, är den mellan väteisotoperna deuterium (d) och tritium (t). Dessa fusionerar enligt reaktionen $d + t \rightarrow {}^4\text{He} + n$, där n är en neutron. I denna reaktion frigörs nästan 18 MeV ($3 \cdot 10^{-12}$ J), där neutronenergin är 14 MeV.

För att dessa reaktioner ska kunna ske måste deuterium- och tritiumkärnornas energi vara större än Coulumbbarriären som finns mellan dem på grund av deras laddning. Detta kan ske genom att upphetta en gas av deuterium och tritium till 10^8 °C. En gas med så hög temperatur är i plasmaform, det vill säga elektroner och kärnor (joner) är helt särkopplade från varandra. För att bibehålla plasmats temperatur är det viktigt att det inte växelverkar med andra material. Detta kan lösas just på grund av att den varma gasen är i plasmaform. Vi kan använda oss av att partiklar som befinner sig i magnetfält roterar runt magnetfältets linjer. I en tokamak innesluter man ett plasma genom att skapa ett badringsformat magnetfält.

Men neutroner är neutrala och följaktligen kommer de inte stoppas av tokamakens magnetfält. Detta är ett problem eftersom så högenergetiska neutroner kommer aktivera det material som omger vårt plasma. Å andra sidan, kan man utnyttja neutronstrålningen dels för att skapa mer tritium genom reaktionen $n + \text{Li} \rightarrow t + \alpha$ och dels för att diagnostisera plasmat. Diagnostiseringen kan ske eftersom neutronenergierna kommer vara beroende av jonenergifördelningarna inne i plasmat

Den här avhandlingen behandlar olika mättekniker för att mäta energifördelningen som neutronerna har när de lämnat plasmat. Framförallt beskrivs den magnetiska protonrekylspektrometern (MPR). MPR:n har ett kollimerat neutronflöde riktat mot sig. Dessa neutroner passerar ett tunt (väterikt) plastfolie. En liten andel av neutronerna sprids elastiskt mot vätekärnorna i foliet, vilket får som följd att rekylprotoner kommer spridas från foliet. Protonenergierna, E_p , kommer vara

$$E_p = E_n \cos^2(\theta), \quad (6.1)$$

där E_n motsvarar neutronenergin och θ är spridningsvinkel mellan neutronens och protonens hastighet. De protoner som sprids framåt (och har ungefär samma energi som neutronen) släpps in i ett specialdesignat magnetfält som böjer av protonerna från neutronstrålen. I magnetfältet blir protonerna rumsligt rörelsemängdseparerade med hjälp av Lorentzkraften. I fokuset av magnetfältet finns en segmenterad protondetektor som mäter den rumsliga fördelningen av protonerna. Denna fördelning kan sen användas för att räkna ut neutronernas ursprungliga energi.

Denna avhandling har undersökt effekterna av en uppgradering av MPR (MPRu) och kvantifierat egenskaper hos spektrometern, såsom till exempel instrumentets energiupplösning och effektivitet och dessa två parametrars systematiska osäkerheter.

Utöver instrumenteringen av MPRu har denna avhandling använt syntetiska data, dels för att undersöka avfaltningskoder, och dels för att undersöka olika neutronspektrometertekniker på ITER. Avfaltningskoderna har undersökts kvantitativt genom att falta de syntetiska data, motsvarande olika neutronspektrum, med responsfunktioner för olika spektrometrar. Detta resulterar i syntetiska mätningar. Ett statistiskt brus läggs nu till den syntetiska lösningen för att simulera en realistisk mätning. Koderna får sedan avfalta dessa syntetiska data för att försöka återskapa det ursprungliga syntetiska neutronspektrumet.

En del av arbetet med spektrometertekniker på ITER har varit att simulera och/eller samla in mätningar som bygger upp responsfunktionerna som beskriver mätprocesserna för de olika teknikerna. När detta var gjort användes syntetiska data återigen för att uppskatta med vilken tidsupplösning man kan mäta olika plasmamparametrar, såsom till exempel jontemperaturen. Resultatet av denna utvärdering är att tekniker som baseras på tunnfolietekniken, såsom till exempel MPRu, ger bäst tidsupplösning.

7. Acknowledgements

There are so many people that deserve thanks for helping me during my time as a PhD student. This work has truly been a group effort. I hope you know how grateful I am to you. If you don't, I will try to explain it in this chapter.

First of all I would like to thank my main supervisor, Göran. This thesis would not be what it is without your knowledge and the thorough input you have given to the data analysis, scientific writing and simulations. I am so grateful for all the things you have taught me. Secondly, co-supervisor Sean deserves my deepest gratitude for teaching me so much about physics and programming. Furthermore, I am grateful to you for introducing me to the path of Python, which I might never leave, and all the Sci-Fi series that you know by heart.

Henrik, all the time we've spent together has been great, including the nights spent characterizing the phoswich detectors and all the evenings spent together in Abingdon. I guess your theories will never stop to amaze me. The MPRu team rocks! Maria, all the work related chats have been very helpful. However, thinking back at this time I will rather remember the first shared office (10 m²), the coffee, the support when needed and all our laughs. It has meant a lot. Carl, despite the secrets of yours, I will always be grateful for all the time you have helped me out with everything from programming to explaining weird physics parameters such as ρ^* .

Luca, all our nightly talks in Abingdon will always be remembered. Anders, thanks for always having some spare time to explain. Lele, all the unfolding discussions have really deepened my understanding on the matter. As soon as your parameterised models of the camera data is implemented for D data I will phone you! Matthias, we have not spent so much time together as researchers, but the more as teachers. The first "Energy physics" course together was an achievement to remember. Marco T, Massimo and Giuseppe, your enthusiastic involvement in the fusion group's research here in Uppsala is valuable. Marco C and Siriyaporn, your work on the MAST camera is both inspiring and impressing in terms of efficiency and organisation. Keep up the good work!

There are so many people that deserve thanks at the department. All the good coffee times and all the discussion about everything, has made life at the department great fun. Thank you all co-workers!

My deepest gratitude goes to my big and loving family. Mom and Dad, thank you for always supporting me and always being around when needed. My sister and brothers, I can't even imagine life without you. I expect you to

call me “Doktor Erik” from now on. Therese, without your love I would not have made this. I am so grateful for all the things you do - the support, the comfort and your laughs. Gustav, att komma hem till dig på kvällarna efter en utmattande arbetsdag får mig alltid på gott humör. Du gör mig till en bättre människa! My/Elias, trots att du inte kommit till oss än har jag redan anledning att tacka dig för att du väntade med att komma ut tills denna avhandling var färdigskriven.

Bibliography

- [1] J. Wesson. *Tokamaks*. Oxford Science Publications, 3rd edition, 1999.
- [2] J. Wesson. *The science of JET*. Pre-Print. JET-R(99)13, 1999.
- [3] M. Keilhacker. JET Deuterium-Tritium results and their implications. *JET Pre-Print. JET-P(98)70*, 1998.
- [4] Home page of ITER. <http://www.iter.org>.
- [5] L. Bertalot et al. Calibration of the JET neutron activation system for DT operation. *Rev. Sci. Instrum.*, 70:1137, 1999.
- [6] C.W. Barnes et al. Operation and cross calibration of the activation foil system on TFTR. *Rev. Sci. Instrum.*, 61:3190, 1990.
- [7] M. Hoek et al. Neutron yield measurements by use of foil activation at JT-60U. *Rev. Sci. Instrum.*, 66:885–887, 1995.
- [8] O.N. Jarvis et al. Calculation and measurements of ^{235}U and ^{238}U fission counter assembly detection efficiency. *Rev. Sci. Instrum.*, 61:3172–3174, 1990.
- [9] D.L. Jassby et al. Absolute calibration of tokamak fusion test reactor neutron detectors for D-T plasma operation. *Rev. Sci. Instrum.*, 66:3172–3174, 1995.
- [10] T. Nishitani et al. Absolute calibration of the JT-60U neutron monitors using a ^{252}Cf neutron source. *Rev. Sci. Instrum.*, 63:5270–5278, 1992.
- [11] J.M. Adams et al. The JET neutron emission profile monitor. *Nucl. Instrum. Meth. A*, 329:277–290, 1993.
- [12] A. L. Roquemore et al. TFTR multichannel neutron collimator. *Rev. Sci. Instrum.*, 61:3163–3165, 1990.
- [13] M. Ishikawa et al. First measurement of neutron emission profile on JT-60U using stilbene neutron detector with neutron-gamma discrimination. *Rev. Sci. Instrum.*, 73:4237–, 2002.
- [14] E. Ronchi et al. Neural networks based neutron emissivity tomography at JET with real-time capabilities. *Nucl. Instrum. Meth. A*, 613:295–303, 2009.
- [15] L. Ingesson et al. Soft X ray tomography during ELMs and impurity injection in JET. *Nucl. Fusion*, 38:1675, 1998.

- [16] H. Brysk. Fusion neutron energies and spectra. *Plasma Physics*, 15:611–617, 1972.
- [17] C. Hellesen et al. Validating TRANSP simulations using neutron emission spectroscopy with dual sight lines. *Rev. Sci. Instrum.*, 79, 2008.
- [18] M. Tardocchi et al. Ion temperature and plasma rotation profile effects in the neutron emission spectrum. *Rev. Sci. Instrum.*, 75:661–668, 2004.
- [19] A.J.H. Donné et al. Silicon surface barrier detector for fusion neutron spectroscopy. *Nucl. Fusion*, 47:S337, 2007.
- [20] B. Esposito et al. Digital pulse shape discrimination in organic scintillators for fusion applications. *Nucl. Instrum. Meth. A.*, 518:626–628, 2004.
- [21] D. Marocco et al. High count rate neutron spectrometry with liquid scintillation detectors. *IEEE Nucl. Sci.*, 56:1168–1173, 2009.
- [22] B. Esposito et al. Neutron measurements on Joint European Torus using an NE213 scintillator with digital pulse shape discrimination. *Rev. Sci. Instrum.*, 75:3550–3552, 2004.
- [23] Yu.A.Kaschuck et al. Neutron measurements during Trace Tritium Experiments at JET using a stilbene detector. *31st EPS Conference on Plasma Phys. London*, pages P–5.174, 2004.
- [24] A. Zimbal et al. Compact NE213 neutron spectrometer with high energy resolution for fusion applications. *Rev. Sci. Instrum.*, 75:3553, 2004.
- [25] T. Elevant et al. Silicon surface barrier detector for fusion neutron spectroscopy. *Rev. Sci. Instrum.*, 57:1763–1765, 1986.
- [26] S. Conroy et al. Time resolved measurements of triton burnup in jet plasmas. *Nucl. Fusion*, 28:2127–2133, 1988.
- [27] M. Pillon et al. 14 MeV neutron spectra measurements using II^a diamonds detectors. *Rad. Prot. Dosimetry*, 66:371–374, 1996.
- [28] A.V. Krasilnikov et al. TFTR natural diamond detectors based D–T neutron spectrometry system. *Rev. Sci. Instrum.*, 68:553, 1997.
- [29] G.J. Schmid et al. A neutron sensor based on single crystal CVD diamond. *Nucl. Instrum. and Meth. A*, 527:554–561, 2004.
- [30] A.V. Krasilnikov et al. Fusion neutronic source deuterium–tritium neutron spectrum measurements using natural diamond detectors. *Rev. Sci. Instrum.*, 68:1720, 1997.
- [31] A.V. Krasilnikov et al. Study of d–t neutron energy spectra at jet using natural diamond detectors. *Nucl. Instrum. And Meth. A*, 476:500, 2002.

- [32] M. Isobe et al. First measurement of neutron emission profile on JT-60U using stilbene neutron detector with neutron-gamma discrimination. *Fusion Engi. and Des.*, 34-35:573, 1997.
- [33] T. Elefant et al. Fusion neutron energy spectra measured by time-of-flight spectrometers. *Nucl. Instrum. and Meth. A*, 476:485, 2002.
- [34] O.N. Jarvis. Neutron spectrometry at JET (1983–1999). *Nucl. Instrum. Meth. A*, 476:474–484, 2002.
- [35] M. Gatu Johnson et al. The 2.5-MeV neutron time-of-flight spectrometer TOFOR for experiments at JET. *Nucl. Instrum. Meth. A*, 591:417–430, 2008.
- [36] Y. Shibata et al. Time-of-flight neutron spectrometer for JT-60U. *Rev. Sci. Instrum.*, 72:828, 2001.
- [37] N.P. Hawkes et al. A 14 MeV neutron spectrometer for the joint european torus deuterium-tritium experiments. *Rev. Sci. Instrum.*, 70:1134, 1999.
- [38] S. Conroy et al. Neutron spectrometer for iter using silicon detectors. *Rev. Sci. Instrum.*, 79:10E508, 2008.
- [39] N.P. Hawkes et al. Neutron spectrometry for d–t plasmas in jet, using a tandem annular-radiator proton-recoil spectrometer. *Nucl. Instrum. Meth. A*, 476:490–494, 2002.
- [40] N.P. Hawkes et al. The design of a proton recoil telescope for 14 mev neutron spectrometry. *Nucl. Instrum. Meth. A*, 476:506–510, 2002.
- [41] W. Cash et al. Parameter estimation in astronomy through application of the likelihood ratio. *Astrophys. Journal*, 228:939, 1979.
- [42] Private communication with C. Hellesen.
- [43] H. Sjöstrand et al. Triton burn up neutron emission in JET low current plasmas. *Journal of Phys. D: Applied Phys.*, 57:162–175, 2008.
- [44] C. Hellesen et al. Neutron emission generated by fast deuterons accelerated with ion cyclotron heating at JET. *Nucl. Fusion*, 50:022001, 2010.
- [45] H. Sjöstrand et al. Fusion power measurement using a combined neutron spectrometer-camera system at JET. *Fusion Sci. and Techn.*, 57:162–175, 2010.
- [46] L.L. Lao et al. *Nucl. Fusion*, 25:1421, 1985.
- [47] D.P. O’Brien et al. Equilibrium analysis of iron core tokamaks using a full domain method. *Nucl. Fusion*, 32:1351, 1992.
- [48] D.B. Pelowitz (edited by). MCNPX user’s manual. Technical report, Los Alamos National Laboratory, 2005. Version 2.5.0, LA-CP-05-0369.
- [49] J. Ongena. *Trans. of Fusion Technology*, 33:181, 1998.

- [50] E. Ronchi et al. A parametric model for fusion neutron emissivity tomography for the KN3 neutron camera at JET. *Nucl. Fusion*, 50:035008, 2010.
- [51] E.A. Belogorlov et al. Interpretation of the solution to the inverse problem for the positive function and the reconstruction of neutron spectra. *Nucl. Instrum. Meth. A*, 235:146–163, 1985.
- [52] M. Reginatto et al. MAXED, a computer code for the deconvolution of multi-sphere data using the maximum entropy method. Technical report, Environmental Measurements Laboratory, 1998. Report EML-595.
- [53] J. Mlynar et al. Neutron spectra unfolding with Minimum Fisher Regularisation. *Proceedings of Science*, 2006.
- [54] M. Reginatto et al. Bayesian and maximum entropy methods for fusion diagnostic measurements with compact neutron spectrometers. *Rev. Sci. Instrum.*, 79:023505, 2008.
- [55] P.C. Hansen. Analysis of discrete ill-posed problems by means of the l-curve. *SIAM review*, 34:561–580, 1992.
- [56] M. Shimada et al. Progress in the ITER physics basis Chapter 1: Overview and summary. *Nucl. Fusion*, 47:S1, 2007.
- [57] C. Gormezano et al. Progress in the ITER physics basis Chapter 6: Steady state operation. *Nucl. Fusion*, 47:S285, 2007.

Acta Universitatis Upsaliensis

*Digital Comprehensive Summaries of Uppsala Dissertations
from the Faculty of Science and Technology 726*

Editor: The Dean of the Faculty of Science and Technology

A doctoral dissertation from the Faculty of Science and Technology, Uppsala University, is usually a summary of a number of papers. A few copies of the complete dissertation are kept at major Swedish research libraries, while the summary alone is distributed internationally through the series Digital Comprehensive Summaries of Uppsala Dissertations from the Faculty of Science and Technology. (Prior to January, 2005, the series was published under the title "Comprehensive Summaries of Uppsala Dissertations from the Faculty of Science and Technology".)



ACTA
UNIVERSITATIS
UPSALIENSIS
UPPSALA
2010

Distribution: publications.uu.se
urn:nbn:se:uu:diva-121615